ELSEVIER

Finite Elements in Analysis and Design 33 (1999) 283–315

FINITE ELEMENTS IN ANALYSIS AND DESIGN

www.elsevier.com/locate/finel

A finite element model of localized deformation in frictional materials taking a strong discontinuity approach

Richard A. Regueiro*, Ronaldo I. Borja

Department of Civil and Environmental Engineering, Stanford University, Stanford, CA 94305-4020, USA

Abstract

A finite element model of localized deformation in frictional materials taking a strong discontinuity approach is presented. A rate-independent, non-associated, strain-softening Drucker–Prager plasticity model is formulated in the context of strong discontinuities and implemented along with an enhanced quadrilateral element within the framework of an assumed enhanced strain finite element method. For simple model problems such as uniform compression, the strong discontinuity approach has been shown to lead to mesh-independent finite element solutions when localized deformation is present. In this paper, a finite element analysis of localized deformation occurring in a more complex model problem of slope stability is conducted in a nearly mesh-independent manner. The effect of dilatancy on the orientation of slip lines is demonstrated for the slope stability problem. © 1999 Elsevier Science B.V. All rights reserved.

1. Introduction

Localized deformation in the form of slip surfaces and shear bands occurs naturally in frictional materials such as soil and rock. As a result, in order for the geotechnical engineer or engineering geologist to make informed analysis and design decisions for geomechanical structures in which localized deformation may develop, slip surfaces and shear bands should be represented numerically by a finite element model. The usefulness of a finite element model is realized when analyzing geomechanical structures with complex geometry and material behavior because for such problems an analytical limit equilibrium solution is unwieldy [1,2].

There have been numerous experimental studies of the physical phenomenon of localized deformation in frictional materials such as soil and rock by Vardoulakis et al. [3], Vardoulakis and

* Corresponding author. Sandia National Laboratories, P.O. Box 969, MS 9405, Livermore, CA 94551-0969, USA.
E-mail address: raregue@sandia.gov (R.A. Regueiro)

0168-874X/99/$ - see front matter © 1999 Elsevier Science B.V. All rights reserved.
PII: S0168-874X(99)00050-5

Goldschieder [4], Hallbauer et al. [5], Santarelli and Brown [6], Wawersik et al. [7], Ord et al. [8], Yumlu and Ozbay [9], and Labuz et al. [10], to name a few (see Read and Hegemier [11] for a review). Many of these studies have attempted to understand the connection between the microscopic actions (e.g., micro-cracking in brittle rock, mineral particle rolling and sliding in granular soil, and mineral particle rotation and translation in the cement matrix of soft rock) and the macroscopic behavior (e.g., formation of slip surfaces and shear bands and progressive loss of overall material body strength). A number of microscopic-based numerical models of localized deformation in granular materials have been considered to attempt to establish this connection numerically [12–16]. This paper, on the other hand, discusses a macroscopic approach to modeling localized deformation via the finite element method.

Concurrent with the appearance of localized deformation is the loss of overall strength of the frictional material body. Typically, rate-independent strain-softening plasticity models have been used to represent this overall 'softening' behavior in frictional materials like soil and rock [17]. It is well-known, however, that rate-independent strain-softening plasticity models lead to mesh-dependent finite element solutions because such models do not contain a material length scale needed to define the width of a localized deformation zone and because the associated governing partial differential equation is ill-posed [18]. In addition, the mesh alignment of standard finite elements has been shown to affect the simulated localized deformation pattern. Therefore, a more sophisticated numerical tool to represent the formation of slip surfaces and shear bands in frictional materials like soil and rock in a mesh-independent manner is in order.

The phenomenon of localized deformation has been studied as a material instability leading to a bifurcation in solution of the initial boundary value problem [19–23]. These works laid the foundation for determining a localization condition which detects the bifurcation point of solution, a condition used by many numerical modelers to determine when to include enhancements to the finite element displacement or strain interpolations. In this paper, we use a model which leads to a bifurcated solution. This model will be introduced after a brief discussion of other numerical models which have been developed to simulate localized deformation.

Many attempts have been made to numerically model localized deformation using rate-independent, strain-softening plasticity models, but, in the absence of a material 'length scale', adaptive remeshing, or another regularization technique, these attempts typically do not satisfy two necessary criteria for a finite element solution to be meaningful (i.e., mesh-independent): objectivity with respect to mesh refinement and insensitivity to mesh alignment. The length-scale approach for modeling localized deformation in a manner independent of element size was considered by Pietruszczak and Mróz [24], Bažant and Lin [25], and Oliver [26], among others. The basic idea of incorporating a material length scale within the constitutive model and/or at the finite element level is to fix the width of the localized deformation zone since rate-independent plasticity models do not provide this information. Essentially, the introduction of a material length scale precludes a causal a priori-defined length scale of the associated mesh-size pathology; this a priori-defined length scale takes the form of the finite element diameter. From a purely numerical perspective, the adaptive remeshing approach for modeling localized deformation was considered by Zienkiewicz and Huang [27] and Zienkiewicz et al. [28], among others. This approach does not consider local material instability but addresses the phenomenon of localized deformation solely via adaptive mesh strategies. The difficulty with this approach is that one needs to refine the mesh to the 'fine

scale' of the physical manifestation of localized deformation in order to adequately represent the phenomenon. It would thus be more attractive to incorporate this 'fine scale' into a 'coarse scale' like a finite element mesh through a multiscale approach [29,30]. The length-scale approach is multiscale but requires the ad hoc introduction of a material length scale and also typically does not sharply capture the orientation of the localized deformation pattern, unless combined with an enhanced finite element method like that of Ortiz et al. [31] or Belytschko et al. [32]. On the other hand, it has been shown that rate-dependent plasticity models contain an implicit length scale which regularizes the mesh pathology associated with the rate-independent limit [18,33–37]. Here, though, it is of interest to consider the rate-independent case directly. Other models which contain an implicit length scale are the higher-order gradient plasticity models [38,39] and the micropolar continuum models [40–42].

A previously developed model which falls under the rubric of 'multiscale approach' represents localized deformation as a strong discontinuity (jump in displacement field) and is called the *strong discontinuity approach* in this paper. The strong discontinuity approach referred to in this paper is that developed by Simo and co-workers [43–47] and yields mesh-independent finite element solutions without introducing a material length scale and without requiring special mesh alignment strategies. There have been other strong discontinuity approaches by Wan et al. [48], Larsson et al. [49,50] in the sense that displacement jumps are treated directly rather than smeared into weak discontinuities (jump in strain field; see [51]). The strong discontinuity approach by Simo and co-workers is adopted in this work to formulate a rate-independent, non-associated, strain-softening Drucker–Prager plasticity model in the context of strong discontinuities and to implement this plasticity model along with an enhanced quadrilateral element within the framework of an assumed enhanced strain finite element method [52,53]. The formulation and implementation are carried out for small deformations and rotations, and under drained condition (whereby the effect of pore-fluid influence is neglected) and quasi-static loading.

The presentation of this paper proceeds as follows: Section 2 establishes the governing equations of quasi-static equilibrium for an isothermal solid with discontinuity; Section 3 defines the kinematics of strong discontinuities; Section 4 outlines a standard, general non-associated plasticity model; Section 5 discusses the derivation of a general non-associated plasticity model with strong discontinuity; Section 6 particularizes the results in Section 5 for a Drucker–Prager plasticity model; Section 7 delineates the finite element implementation; Section 8 presents a numerical simulation of localized deformation in a slope; and Section 9 closes the paper.

2. Governing equations with discontinuity

Consider a closed body $\bar{\Omega} \subset \mathbb{R}^{n_{\text{dim}}}(n_{\text{dim}} = 1, 2, \text{or } 3)$ with smooth (i.e. C^1) internal discontinuity surface $\mathscr{S} \subset \mathbb{R}^{n_{\text{dim}}-1}$ as shown in Fig. 1. Let $\boldsymbol{x} \in \Omega$ denote the location of material particles $\boldsymbol{x}$ in Ω.

The local (strong) form of the quasi-static, isothermal equilibrium equations may be expressed as follows [54]: Given $\boldsymbol{b} : \Omega \to \mathbb{R}^{n_{\text{dim}}}$, $\boldsymbol{t} : \partial_t\Omega \to \mathbb{R}^{n_{\text{dim}}}$, and $\boldsymbol{g} : \partial_u\Omega \to \mathbb{R}^{n_{\text{dim}}}$, find $\boldsymbol{u} : \bar{\Omega} \times [0, T] \to \mathbb{R}^{n_{\text{dim}}}$ (where $[0, T] \subset \mathbb{R}_+$ is the time interval of interest) such that

$$\boldsymbol{V} \cdot \boldsymbol{\sigma} + \boldsymbol{b} = \boldsymbol{0} \quad \text{in } \Omega,$$

$$\boldsymbol{\sigma} \cdot \boldsymbol{v} = \boldsymbol{t} \quad \text{on } \partial_t\Omega,$$

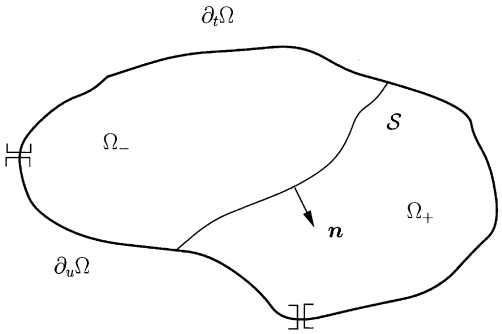

Fig. 1. Body $\bar{\Omega}$ with discontinutiy $\mathcal{S}(\Omega = \Omega_+ \cup \Omega_-, \partial\Omega = \partial_t\Omega \cup \partial_u\Omega \cup \mathcal{S}, \bar{\Omega} = \Omega \cup \partial\Omega)$.

$$\boldsymbol{u} = \boldsymbol{g} \quad \text{on } \partial_u\Omega,$$
$$[\![\boldsymbol{\sigma}]\!] \cdot \boldsymbol{n} = [\![\boldsymbol{t}_{\mathcal{S}}]\!] = \boldsymbol{0} \quad \text{across } \mathcal{S}, \tag{1}$$

where $\boldsymbol{\sigma}$ is the Cauchy stress, $\boldsymbol{b}$ is the prescribed body force, $\boldsymbol{v}$ is the unit normal to $\partial_t\Omega$, $\boldsymbol{n}$ is the unit normal to $\mathcal{S}$, $\boldsymbol{t}$ is the prescribed traction, $\boldsymbol{g}$ is the prescribed displacement, and $[\![\bullet]\!]$ denotes the jump of a quantity across $\mathcal{S}$ (i.e. $[\![\boldsymbol{\sigma}]\!] = \boldsymbol{\sigma}^+ - \boldsymbol{\sigma}^-$). Refer to Malvern [55, p. 242] for a brief discussion of discontinuity surfaces and their effect on the variational form of equilibrium.

The variational (weak) form of the quasi-static equilibrium equations, using the strong form as a point of departure (or vice versa), may be expressed as follows [54]: Given $\boldsymbol{b} : \Omega \to \mathbb{R}^{n_{\text{dim}}}$, $\boldsymbol{t} : \partial_t\Omega \to \mathbb{R}^{n_{\text{dim}}}$, and $\boldsymbol{g} : \partial_u\Omega \to \mathbb{R}^{n_{\text{dim}}}$, find $\boldsymbol{u} \in \mathscr{U}$ such that for all $\boldsymbol{\eta} \in \mathscr{V}$,

$$\int_\Omega \nabla^s\boldsymbol{\eta} : \boldsymbol{\sigma}\,\mathrm{d}\Omega = \int_\Omega \boldsymbol{\eta}\cdot\boldsymbol{b}\,\mathrm{d}\Omega + \int_{\partial_t\Omega} \boldsymbol{\eta}\cdot\boldsymbol{t}\,\mathrm{d}\Gamma + \int_{\mathcal{S}} \boldsymbol{\eta}\cdot([\![\boldsymbol{\sigma}]\!]\cdot\boldsymbol{n})\,\mathrm{d}\Gamma, \tag{2}$$

where $\boldsymbol{\eta}$ is the weighting function. The space of admissible weighting functions is

$$\mathscr{V} := \{\boldsymbol{\eta} : \Omega \to \mathbb{R}^{n_{\text{dim}}};\ \boldsymbol{\eta} = \boldsymbol{0} \text{ on } \partial_u\Omega\}, \tag{3}$$

and the space of admissible trial solutions is defined as

$$\mathscr{U} := \{\boldsymbol{u} : \bar{\Omega} \to \mathbb{R}^{n_{\text{dim}}};\ \boldsymbol{u} = \boldsymbol{g} \text{ on } \partial_u\Omega\}. \tag{4}$$

Notice that in Eq. (2) traction continuity across the discontinuity surface $\mathcal{S}$ is required for equilibrium to be satisfied.

3. Kinematics of strong discontinuities

It was proven for rate-independent, infinitesimal, perfect plasticity that discontinuous displacement fields are admissible solutions to the boundary value problem and are contained within the bounded deformation (BD) space (see [56–59]). The infinitesimal strains are singular distributions, which are contained within the space of bounded measures because the integral of the Dirac-delta

function is a finite measurable quantity. A localization condition is formulated in Section 5.4 which detects the inception of such discontinuous displacements.

Define the discontinuous displacement field as follows:

$$\boldsymbol{u}(\boldsymbol{x},t) = \underbrace{\bar{\boldsymbol{u}}(\boldsymbol{x},t)}_{\text{continuous}} + \underbrace{[\![\boldsymbol{u}(t)]\!]H_{\mathscr{S}}(\boldsymbol{x})}_{\text{discontinuous}}, \tag{5}$$

where $[\![\boldsymbol{u}]\!] = \boldsymbol{u}^+ - \boldsymbol{u}^- = \zeta\boldsymbol{m}$ is the jump in displacement across the discontinuity surface $\mathscr{S}$ and is assumed independent of $\boldsymbol{x}$, ζ is the jump magnitude, $\boldsymbol{m}$ is the unit vector designating the jump direction, and $H_{\mathscr{S}}(\boldsymbol{x})$ is the Heaviside function defined as

$$H_{\mathscr{S}}(\boldsymbol{x}) = \begin{cases} 1 & \text{if } \boldsymbol{x} \in \Omega_+, \\ 0 & \text{if } \boldsymbol{x} \in \Omega_-. \end{cases} \tag{6}$$

It is possible for $[\![\boldsymbol{u}]\!]$ to vary along the discontinuity $\mathscr{S}$, but here it is considered constant with respect to $\boldsymbol{x}$. Taking the symmetric gradient of the displacement field in (5) and treating the Dirac-delta function as a distribution, the small strain tensor results [43]

$$\boldsymbol{\varepsilon} := \boldsymbol{\nabla}^s\boldsymbol{u} = \underbrace{\boldsymbol{\nabla}^s\bar{\boldsymbol{u}}}_{\text{regular}} + \underbrace{([\![\boldsymbol{u}]\!]\otimes\boldsymbol{n})^s\delta_{\mathscr{S}}}_{\text{singular}} \tag{7}$$

where $\boldsymbol{n}$ is the unit normal to the discontinuity surface $\mathscr{S}$ pointing into Ω_+ (see Fig. 1), and $\delta_{\mathscr{S}}$ is the Dirac-delta function on $\mathscr{S}$. Essentially, $\boldsymbol{\nabla}H_{\mathscr{S}} = \boldsymbol{n}\delta_{\mathscr{S}}$. It is important that the Dirac-delta function be treated in the distributional framework [60] throughout the formulation of a plasticity model with strong discontinuity.

4. Standard non-associated plasticity

Here, a standard non-associated plasticity model is formulated for small deformations and rotations. Refer to Simo and Hughes [61] for a detailed discussion of the formulation and numerical implementation of plasticity models.

Consider a convex elastic domain $\mathbb{E}$ defined by a smooth (i.e. C^1 continuous) yield surface $\phi : \mathbb{S}\times\mathbb{R}^m \to \mathbb{R}$ in the Cauchy stress space $\boldsymbol{\sigma} : \Omega\times[0,T] \to \mathbb{S}$ as

$$\mathbb{E} := \{(\boldsymbol{\sigma},\boldsymbol{\alpha}) \in \mathbb{S}\times\mathbb{R}^m | \phi(\boldsymbol{\sigma},\boldsymbol{\alpha}) \leqslant 0\}, \tag{8}$$

where $[0,T]$ is the time increment of interest, $\mathbb{S}$ is the space of symmetric second-order tensors, and $\boldsymbol{\alpha} : \Omega\times[0,T] \to \mathbb{R}^m$ is the stress-like vector of plastic internal variables of dimension m characterizing the hardening response of the material. The constitutive equation is expressed in terms of a stored energy density function $\Psi(\boldsymbol{\varepsilon}^e,\boldsymbol{\xi}) : \mathbb{S}\times\mathbb{R}^m \to \mathbb{R}$, where $\boldsymbol{\varepsilon}^e : \Omega \to \mathbb{S}$ is the elastic part of the infinitesimal strain tensor, and $\boldsymbol{\xi} : \Omega\times[0,T] \to \mathbb{R}^m$ is the strain-like vector of plastic internal variables, which is (energy) conjugate to $\boldsymbol{\alpha}$. The constitutive equations are then defined via consideration of the first and second laws of thermodynamics in the manner of Lubliner [62] as

$$\boldsymbol{\sigma} = \frac{\partial\Psi(\boldsymbol{\varepsilon}^e,\boldsymbol{\xi})}{\partial\boldsymbol{\varepsilon}^e}, \qquad \boldsymbol{\alpha} = -\frac{\partial\Psi(\boldsymbol{\varepsilon}^e,\boldsymbol{\xi})}{\partial\boldsymbol{\xi}}. \tag{9}$$

For the linearized theory the strain tensor is additively decomposed into elastic and plastic parts:

$$\boldsymbol{\varepsilon} = \boldsymbol{\varepsilon}^{\mathrm{e}} + \boldsymbol{\varepsilon}^{\mathrm{p}}. \tag{10}$$

The plastic strain rate $\dot{\boldsymbol{\varepsilon}}^{\mathrm{p}} : \Omega \times [0, T] \to \mathbb{S}$ is defined via the flow rule as

$$\dot{\boldsymbol{\varepsilon}}^{\mathrm{p}} = \lambda \frac{\partial \varphi(\boldsymbol{\sigma}, \boldsymbol{\alpha})}{\partial \boldsymbol{\sigma}}, \tag{11}$$

where $\lambda : \Omega \times [0, T] \to \mathbb{R}$ is the plastic consistency parameter, and $\varphi(\boldsymbol{\sigma}, \boldsymbol{\alpha}) : \mathbb{S} \times \mathbb{R}^m \to \mathbb{R}$ is the plastic potential function, which is not necessarily equal to $\phi(\boldsymbol{\sigma}, \boldsymbol{\alpha})$. Associative plasticity results if $\partial_{\sigma}\varphi = \partial_{\sigma}\phi$ and associative hardening if $\partial_{\alpha}\varphi = \partial_{\alpha}\phi$. As mentioned previously, for frictional materials like soil and rock, plasticity models are non-associative because the dilation angle is experimentally observed to be less than the friction angle, making $\partial_{\sigma}\varphi \neq \partial_{\sigma}\phi$. Non-associated plasticity models violate Drucker's stability postulate [63], but make physical sense with respect to a calculation of dissipation for a cohesionless, perfectly plastic material [64]. The evolution equations for $\boldsymbol{\varepsilon}^{\mathrm{e}}$ and $\boldsymbol{\xi}$ are defined as

$$\dot{\boldsymbol{\varepsilon}}^{\mathrm{e}} = \dot{\boldsymbol{\varepsilon}} - \lambda \frac{\partial \varphi}{\partial \boldsymbol{\sigma}}, \quad \dot{\boldsymbol{\xi}} = \lambda \frac{\partial \varphi}{\partial \boldsymbol{\alpha}}. \tag{12}$$

The classical Kuhn–Tucker complementary conditions for loading and unloading apply:

$$\lambda \geqslant 0, \quad \phi(\boldsymbol{\sigma}, \boldsymbol{\alpha}) \leqslant 0, \quad \lambda \phi(\boldsymbol{\sigma}, \boldsymbol{\alpha}) = 0 \tag{13}$$

as well as the consistency condition

$$\dot{\phi} = 0, \quad \lambda > 0. \tag{14}$$

Recall the constitutive equations from (9) and express them in rate form as

$$\dot{\boldsymbol{\sigma}} = \boldsymbol{C} : \dot{\boldsymbol{\varepsilon}}^{\mathrm{e}}; \quad \dot{\boldsymbol{\alpha}} = -\boldsymbol{H} \cdot \dot{\boldsymbol{\xi}} \tag{15}$$

where

$$\boldsymbol{C} = \frac{\partial^2 \Psi(\boldsymbol{\varepsilon}^{\mathrm{e}}, \boldsymbol{\xi})}{\partial \boldsymbol{\varepsilon}^{\mathrm{e}} \partial \boldsymbol{\varepsilon}^{\mathrm{e}}}, \quad \boldsymbol{H} = \frac{\partial^2 \Psi(\boldsymbol{\varepsilon}^{\mathrm{e}}, \boldsymbol{\xi})}{\partial \boldsymbol{\xi} \partial \boldsymbol{\xi}} \tag{16}$$

are the symmetric Hessian tensors of $\Psi(\boldsymbol{\varepsilon}^{\mathrm{e}}, \boldsymbol{\xi})$ evaluated with respect to $\boldsymbol{\varepsilon}^{\mathrm{e}}$ and $\boldsymbol{\xi}$, respectively. The fourth-order tensor $\boldsymbol{C}$ is the tangential elastic modulus tensor, and the second-order tensor $\boldsymbol{H}$ is the tangential plastic modulus matrix. From the consistency condition, the plastic consistency parameter is solved as

$$\lambda = \frac{\partial_{\sigma}\phi : \boldsymbol{C} : \dot{\boldsymbol{\varepsilon}}}{\partial_{\sigma}\phi : \boldsymbol{C} : \partial_{\sigma}\varphi + \mathscr{H}}, \tag{17}$$

where

$$\mathscr{H} = \partial_{\alpha}\phi \cdot \boldsymbol{H} \cdot \partial_{\alpha}\varphi. \tag{18}$$

The continuum elastic–plastic tangent modulus tensor may then be derived as

$$\boldsymbol{C}^{\mathrm{ep}} = \boldsymbol{C} - \frac{\boldsymbol{C} : \partial_{\sigma}\varphi \otimes \partial_{\sigma}\phi : \boldsymbol{C}}{\partial_{\sigma}\phi : \boldsymbol{C} : \partial_{\sigma}\varphi + \mathscr{H}}. \tag{19}$$

With the standard, non-associated plasticity model in place, the formulation of this plasticity model in the context of strong discontinuituies will proceed.

5. Non-associated plasticity with strong discontinuity

In this section, plastic dissipation, a stress-displacement relation, and a localization condition will be formulated for a general, non-associated plasticity model with strong discontinuity for small deformations and rotations. In the next section the model will be specialized for a Drucker–Prager plasticity model.

5.1. Localized plastic flow

For hardening, associative plasticity ($\mathscr{H} > 0$ from (18)) λ is regular, and the setting for standard plasticity holds. For softening or perfect associative plasticity ($\mathscr{H} \leqslant 0$), however, it is possible for displacements to be discontinuous and for λ to be singular; note that — although not rigorously proven in the manner of [56] — discontinuous displacements may be detected via the localization condition for non-associative hardening plasticity. When discontinuous displacements are present within a material body (detected via the localization condition in Eq. (37)), the strains are singular at the discontinuity $\mathscr{S}$, plastic flow is localized to the discontinuity $\mathscr{S}$ [43], and the plastic consistency parameter λ is a singular distribution

$$\lambda = \lambda_\delta \delta_\mathscr{S}. \tag{20}$$

Eq. (20) states that all further irrecoverable deformation occurs along the discontinuity $\mathscr{S}$ as the body outside the discontinuity unloads elastically. Eq. (20) is the key to a formulation of non-associated plasticity with strong discontinuity.

5.2. Plastic dissipation

A derivation of plastic dissipation with strong discontinuity yields an important quality of the strong discontinuity model.

Recall the definition of plastic dissipation resulting from the second law of thermodynamics in the form of the Clausius–Duhem inequality for an isothermal solid [62,65]:

$$\mathscr{D} := \boldsymbol{\sigma} : \dot{\boldsymbol{\varepsilon}} - \dot{\Psi}(\boldsymbol{\varepsilon}^e, \boldsymbol{\xi}). \tag{21}$$

The rate of dissipation then becomes

$$\mathscr{D} = \lambda(\boldsymbol{\sigma} : \partial_{\boldsymbol{\sigma}} \varphi + \boldsymbol{\alpha} \cdot \partial_{\boldsymbol{\alpha}} \varphi) = \mathscr{D}_\delta \, \delta_\mathscr{S} \tag{22}$$

since $\lambda = \lambda_\delta \delta_\mathscr{S}$. The rate of dissipation is a density quantity, and, as a result, the total rate of dissipation over a region Ω is calculated as

$$\mathscr{D}_\Omega = \int_\mathscr{S} \lambda_\delta (\boldsymbol{\sigma} : \partial_{\boldsymbol{\sigma}} \varphi + \boldsymbol{\alpha} \cdot \partial_{\boldsymbol{\alpha}} \varphi) \, \mathrm{d}\Gamma. \tag{23}$$

Notice that the total rate of dissipation is calculated over a set of zero measure, the discontinuity surface $\mathscr{S}$.

The stress-like vector of plastic internal variables $\boldsymbol{\alpha}$ is a regular function along with the stress tensor $\boldsymbol{\sigma}$. As a result, a calculation of dissipation in Eq. (22) is valid (i.e., no squares of Dirac-delta functions). A key implication on the softening modulus matrix also results. From Eqs. (15) and (20), $\dot{\boldsymbol{\alpha}}$ may be written as

$$\boldsymbol{H}^{-1}\cdot\dot{\boldsymbol{\alpha}} = -\lambda_\delta \partial_{\boldsymbol{\alpha}}\varphi\delta_{\mathscr{S}}. \tag{24}$$

A significant observation made in Simo et al. [43] states that since $\dot{\boldsymbol{\alpha}}$ is regular, the inverse of the softening modulus matrix must itself be a singular distribution

$$\boldsymbol{H}^{-1} = \boldsymbol{H}_\delta^{-1}\delta_{\mathscr{S}} \tag{25}$$

which states that softening is localized to the discontinuity $\mathscr{S}$. As a result of Eq. (25), the following form results for the regular stress-like vector of plastic internal variables:

$$\dot{\boldsymbol{\alpha}} = -\lambda_\delta \boldsymbol{H}_\delta\cdot\partial_{\boldsymbol{\alpha}}\varphi. \tag{26}$$

Thus, as a result of $\lambda = \lambda_\delta\delta_{\mathscr{S}}$, the evolution of the internal variables is localized to the discontinuity $\mathscr{S}$. This result of the strong discontinuity approach could be viewed as a rather 'strong' approximation for some materials (i.e. those which exhibit shear bands of finite width), in the sense that irrecoverable deformation is most likely not completely localized to a surface (except possibly for brittle rock, in which a clear rupture surface is present [7]).

A finite element model which draws its constitutive behavior from a plasticity model with strong discontinuity will calculate mesh-independent dissipation because the total rate of dissipation is calculated over a set of zero measure and not over any a priori-defined finite element diameter.

5.3. Consistency condition and stress–displacement relation

From the previous discussion on plastic dissipation, note that $\dot{\boldsymbol{\sigma}}$ and $\dot{\boldsymbol{\alpha}}$ are regular distributions in order for a calculation of plastic dissipation to be possible, which also implies that the consistency condition $\dot{\phi} = 0$ is satisfied pointwise (i.e. contains no singularities). Employing the chain rule, the consistency condition is

$$\dot{\phi} = \partial_{\boldsymbol{\sigma}}\phi : \dot{\boldsymbol{\sigma}} + \partial_{\boldsymbol{\alpha}}\phi\cdot\dot{\boldsymbol{\alpha}} = 0. \tag{27}$$

Substituting the regular expressions for $\dot{\boldsymbol{\sigma}}$ (i.e., $\dot{\boldsymbol{\sigma}} = \boldsymbol{C} : \boldsymbol{\nabla}^s\dot{\boldsymbol{u}}$) and $\dot{\boldsymbol{\alpha}}$ into Eq. (27), λ_δ is solved as

$$\lambda_\delta = \mathscr{H}_\delta^{-1}\partial_{\boldsymbol{\sigma}}\phi : \boldsymbol{C} : \boldsymbol{\nabla}^s\dot{\boldsymbol{u}}, \tag{28}$$

where $\mathscr{H}_\delta = \partial_{\boldsymbol{\alpha}}\phi\cdot\boldsymbol{H}_\delta\cdot\partial_{\boldsymbol{\alpha}}\varphi$. An equivalent expression for λ_δ may be found from the requirement that all singularities drop out of the consistency condition:

$$\lambda_\delta = \dot{\zeta}\,\frac{\partial_{\boldsymbol{\sigma}}\phi : \boldsymbol{C} : (\boldsymbol{m}\otimes\boldsymbol{n})^s}{\partial_{\boldsymbol{\sigma}}\phi : \boldsymbol{C} : \partial_{\boldsymbol{\sigma}}\varphi}, \tag{29}$$

where $[\![\dot{\boldsymbol{u}}]\!] = \dot{\zeta}\boldsymbol{m}$. Equating (28) and (29) gives a general expression for the magnitude of the jump displacement rate:

$$\dot{\zeta} = \frac{(\partial_{\boldsymbol{\sigma}}\phi : \boldsymbol{C} : \partial_{\boldsymbol{\sigma}}\varphi)(\partial_{\boldsymbol{\sigma}}\phi : \boldsymbol{C} : \boldsymbol{\nabla}^s\dot{\boldsymbol{u}})}{\mathscr{H}_\delta(\partial_{\boldsymbol{\sigma}}\phi : \boldsymbol{C} : (\boldsymbol{m}\otimes\boldsymbol{n})^s)}. \tag{30}$$

Eq. (30) may be simplified using results from the localization condition.

5.4. Localization condition

Here, a condition which detects the presence of discontinuous displacements is derived and called the localization condition. Eq. (2) showed that for equilibrium to be satisfied, the traction must be continuous across the discontinuity surface $\mathscr{S}$:

$$[\![\dot{\boldsymbol{\sigma}}]\!]\cdot\boldsymbol{n} = [\![\dot{\boldsymbol{t}}_{\mathscr{S}}]\!] = \boldsymbol{0}. \tag{31}$$

This condition that the traction must be continuous across the discontinuity surface $\mathscr{S}$ requires that the traction rate be regular. Write the traction rate as follows:

$$\dot{\boldsymbol{t}} = \dot{\boldsymbol{\sigma}}\cdot\boldsymbol{n} = \boldsymbol{C} : (\dot{\boldsymbol{\varepsilon}} - \lambda\partial_{\boldsymbol{\sigma}}\varphi)\cdot\boldsymbol{n} = \dot{\bar{\boldsymbol{t}}} + \dot{\boldsymbol{t}}_\delta\delta_{\mathscr{S}}, \tag{32}$$

where

$$\dot{\bar{\boldsymbol{t}}} = \boldsymbol{C} : \boldsymbol{\nabla}^s\dot{\boldsymbol{u}}\cdot\boldsymbol{n} \tag{33}$$

is the regular part, and

$$\dot{\boldsymbol{t}}_\delta = \dot{\zeta}\boldsymbol{C}^{\mathrm{ep}} : (\boldsymbol{m}\otimes\boldsymbol{n})^s\cdot\boldsymbol{n} \tag{34}$$

is the singular part (using λ_δ from Eq. (29)), with

$$\boldsymbol{C}^{\mathrm{ep}} = \boldsymbol{C} - \frac{\boldsymbol{C} : \partial_{\boldsymbol{\sigma}}\varphi\otimes\partial_{\boldsymbol{\sigma}}\phi : \boldsymbol{C}}{\partial_{\boldsymbol{\sigma}}\phi : \boldsymbol{C} : \partial_{\boldsymbol{\sigma}}\varphi} \tag{35}$$

representing the elastic perfectly plastic tangent modulus tensor. For the traction rate to be regular

$$\dot{\boldsymbol{t}}_\delta = \boldsymbol{0} \tag{36}$$

which leads to the localization condition

$$\boldsymbol{A}\cdot\boldsymbol{m} = \boldsymbol{0}, \quad \boldsymbol{A} = \boldsymbol{n}\cdot\boldsymbol{C}^{\mathrm{ep}}\cdot\boldsymbol{n} \tag{37}$$

where $\boldsymbol{A}$ is the second-order elastic perfectly plastic acoustic tensor. The localization condition requires that $\boldsymbol{m}$ lies in the nullspace of $\boldsymbol{A}$, and likewise that $\boldsymbol{m}\otimes\boldsymbol{n}$ lies in the nullspace of $\boldsymbol{C}^{\mathrm{ep}}$. It is seen that [53]

$$(\boldsymbol{m}\otimes\boldsymbol{n})^s = \Lambda\partial_{\boldsymbol{\sigma}}\varphi \tag{38}$$

where $\Lambda = \lambda_\delta/\dot{\zeta}$; Λ for this analysis can be any real number. It is straightforward to show that $\partial_{\boldsymbol{\sigma}}\varphi$ lies in the nullspace of $\boldsymbol{C}^{\mathrm{ep}}$:

$$\boldsymbol{C}^{\mathrm{ep}} : \partial_{\boldsymbol{\sigma}}\varphi = \boldsymbol{C} : \partial_{\boldsymbol{\sigma}}\varphi - \boldsymbol{C} : \partial_{\boldsymbol{\sigma}}\varphi\,\frac{\partial_{\boldsymbol{\sigma}}\phi : \boldsymbol{C} : \partial_{\boldsymbol{\sigma}}\varphi}{\partial_{\boldsymbol{\sigma}}\phi : \boldsymbol{C} : \partial_{\boldsymbol{\sigma}}\varphi} = \boldsymbol{0}. \tag{39}$$

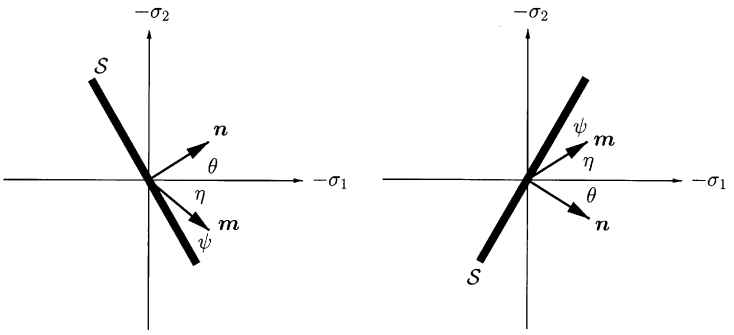

Fig. 2. Slip line orientation with respect to major principal stress axis for $\pm\theta$.

Note that $\boldsymbol{C}^{\mathrm{ep}}$ is the elastic *perfectly plastic* tangent modulus tensor, and thus a derivation of a critical hardening modulus $\mathscr{H}_{\mathrm{cr}}$ similar to that derived by Rudnicki and Rice [66] is not possible. Note that the nullspace of the consistent elastic perfectly plastic tangent modulus tensor $\boldsymbol{C}^{\mathrm{ep}}_{n+1}$ [67] is the same as that of its continuum counterpart $\boldsymbol{C}^{\mathrm{ep}}$ [53]. Also note that the trace of Eq. (38) leads to an expression for the angle made by the jump rate vector $[\![\dot{\boldsymbol{u}}]\!] = \dot{\zeta}\boldsymbol{m}$ and the tangent to the slip line $\mathscr{S}$ (see Fig. 2), called the jump dilation angle ψ:

$$\sin\psi := \boldsymbol{m}\cdot\boldsymbol{n} = \Lambda\,\mathrm{tr}(\partial_{\boldsymbol{\sigma}}\varphi). \tag{40}$$

Eq. (40) will be used to determine the orientation of $\boldsymbol{m}$ when the plastic potential function φ is specified for a particular plasticity model; this will be done for a Drucker–Prager plasticity model. Thus, another way of writing Eq. (30) for $\dot{\zeta}$, using Eq. (28) for λ_δ and Eq. (40) to find $\dot{\zeta}$, is as follows:

$$\dot{\zeta} = \frac{\mathrm{tr}(\partial_{\boldsymbol{\sigma}}\varphi)}{\mathscr{H}_\delta \boldsymbol{m}\cdot\boldsymbol{n}}\,\partial_{\boldsymbol{\sigma}}\phi : \dot{\boldsymbol{\sigma}}. \tag{41}$$

Eq. (41) will be used to derive the stress–displacement relation for a Drucker–Prager plasticity model.

6. Drucker–Prager plasticity with strong discontinuity

The formulation of the preceding section is now specialized for a non-associated Drucker–Prager plasticity model. Such a model is appropriate for modeling the constitutive behavior of frictional materials like soil and rock. First, the standard Drucker–Prager plasticity model is described.

6.1. Standard Drucker–Prager plasticity model

A quadratic stored energy function $\Psi(\boldsymbol{\varepsilon}^{\mathrm{e}}, \boldsymbol{\xi})$, which results in linear elasticity and linear hardening, is defined as

$$\Psi(\boldsymbol{\varepsilon}^{\mathrm{e}}, \boldsymbol{\xi}) := \tfrac{1}{2}\boldsymbol{\varepsilon}^{\mathrm{e}} : \boldsymbol{c}^{\mathrm{e}} : \boldsymbol{\varepsilon}^{\mathrm{e}} + \tfrac{1}{2}\boldsymbol{\xi}\cdot\boldsymbol{H}\cdot\boldsymbol{\xi} \tag{42}$$

where $\boldsymbol{c}^{\mathrm{e}}$ and $\boldsymbol{H}$ are constant modulus tensors. Note that $\Psi(\boldsymbol{\varepsilon}^{\mathrm{e}}, \boldsymbol{\xi})$ could be defined such that nonlinear elasticity and/or hardening would result. The fourth-order tensor $\boldsymbol{c}^{\mathrm{e}}$ is the isotropic elastic tangent modulus tensor defined as

$$\boldsymbol{c}^{\mathrm{e}} = \bar{K}\mathbf{1}\otimes\mathbf{1} + 2\bar{\mu}(\boldsymbol{I} - \tfrac{1}{3}\mathbf{1}\otimes\mathbf{1}) \tag{43}$$

where $\bar{K} = \bar{\lambda} + \frac{2}{3}\bar{\mu}$ is the elastic bulk modulus, $\bar{\lambda}$ and $\bar{\mu}$ are the Lamé parameters, $(\mathbf{1})_{ij} = \delta_{ij}$ is the Kronecker delta, and $(\boldsymbol{I})_{ijkl} = (\delta_{ik}\delta_{jl} + \delta_{il}\delta_{jk})/2$ is the fourth-order identity tensor.

Let the strain-like vector of plastic internal variables $\boldsymbol{\xi} : \Omega \times [0, T] \to \mathbb{R}^2$ have a volumetric component and deviatoric component:

$$\boldsymbol{\xi} := \begin{Bmatrix} v^{\mathrm{p}} \\ e^{\mathrm{p}} \end{Bmatrix}, \tag{44}$$

where

$$\dot{v}^{\mathrm{p}} = \mathrm{tr}(\dot{\boldsymbol{\varepsilon}}^{\mathrm{p}}); \quad \dot{e}^{\mathrm{p}} = \sqrt{\frac{2}{3}}\,\|\dot{\boldsymbol{e}}^{\mathrm{p}}\|; \quad \dot{\boldsymbol{e}}^{\mathrm{p}} = \dot{\boldsymbol{\varepsilon}}^{\mathrm{p}} - (\dot{v}^{\mathrm{p}}/3)\mathbf{1} \tag{45}$$

and

$$v^{\mathrm{p}} = \int_0^T \dot{v}^{\mathrm{p}}\,\mathrm{d}t; \quad e^{\mathrm{p}} = \int_0^T \dot{e}^{\mathrm{p}}\,\mathrm{d}t. \tag{46}$$

The hardening/softening modulus matrix $\boldsymbol{H}$ is defined as

$$\boldsymbol{H} := \begin{bmatrix} K' & 0 \\ 0 & H' \end{bmatrix}, \tag{47}$$

where K' and H' are the bulk and shear hardening/softening moduli, respectively. The stress-like vector of plastic internal variables $\boldsymbol{\alpha}$ is defined as

$$\boldsymbol{\alpha} := \begin{Bmatrix} \alpha_1 \\ \alpha_2 \end{Bmatrix} = -\boldsymbol{H}\cdot\boldsymbol{\xi}. \tag{48}$$

A Drucker–Prager yield function [68] takes the form

$$\phi(\boldsymbol{\sigma}, \boldsymbol{\alpha}) = \sqrt{\tfrac{3}{2}}\|\boldsymbol{s}\| + \sqrt{3}(\kappa + \beta p) = 0 \tag{49}$$

with derivatives

$$\frac{\partial\phi}{\partial\boldsymbol{\sigma}} = \sqrt{\frac{3}{2}}\,\hat{\boldsymbol{n}} + \frac{1}{\sqrt{3}}\beta\mathbf{1}, \quad \frac{\partial\phi}{\partial\boldsymbol{\alpha}} = \begin{Bmatrix} \sqrt{3}b \\ 1 \end{Bmatrix}, \tag{50}$$

where

$$p = \tfrac{1}{3}\mathrm{tr}(\boldsymbol{\sigma}), \quad \boldsymbol{s} = \boldsymbol{\sigma} - p\mathbf{1}, \quad \hat{\boldsymbol{n}} = \boldsymbol{s}/\|\boldsymbol{s}\|, \tag{51}$$

and

$$\kappa := -\bar{\alpha} + b\alpha_1 + \frac{1}{\sqrt{3}}\,\alpha_2 \tag{52}$$

where $\|\boldsymbol{s}\| = \sqrt{s_{ij}s_{ij}}$. Note that for the continuum mechanics convention used throughout this paper, compression implies $p < 0$. The material constants $\bar{\alpha}$ and β may be defined in terms of the cohesion $\bar{c}$ and friction angle $\bar{\phi}$ used to describe a Mohr–Coulomb material [69]

$$\bar{\alpha} = \frac{6\bar{c}\cos\bar{\phi}}{\sqrt{3}(3 + A\sin\bar{\phi})}, \qquad \beta = \frac{6\sin\bar{\phi}}{\sqrt{3}(3 + A\sin\bar{\phi})}, \qquad -1 \leqslant A \leqslant 1. \tag{53}$$

The value $A = -1$ coincides with a cone that circumscribes the Mohr–Coulomb envelope — passing through its outer apexes — in three-dimensional stress space, and $A = 1$ coincides with a cone that passes through the inner apexes of the Mohr–Coulomb envelope. Because of the form of κ in (52), standard bulk and shear hardening/softening through α_1 and α_2 cause the size of the yield cone to change, and not its shape. Incorporating additional hardening/softening through β would allow frictional hardening/softening which is appropriate for modeling a cohesionless granular material like sand, and thus the change of slope of the yield cone would be possible.

A plastic potential function $\varphi(\boldsymbol{\sigma}, \boldsymbol{\alpha})$ is defined similar to the yield function $\phi(\boldsymbol{\sigma}, \boldsymbol{\alpha})$ [70] as

$$\varphi(\boldsymbol{\sigma}, \boldsymbol{\alpha}) = \sqrt{\tfrac{3}{2}}\|\boldsymbol{s}\| + \sqrt{3}(\kappa + bp) \tag{54}$$

with derivatives

$$\frac{\partial\varphi}{\partial\boldsymbol{\sigma}} = \sqrt{\frac{3}{2}}\hat{\boldsymbol{n}} + \frac{1}{\sqrt{3}}\,b\mathbf{1}, \quad \frac{\partial\varphi}{\partial\boldsymbol{\alpha}} = \begin{Bmatrix}\sqrt{3}b\\ 1\end{Bmatrix}, \tag{55}$$

where b is the material dilation constant. Notice that associated plasticity results if $\beta = b$, but typically for soil and rock this is not the case. Usually, $\beta > b$ with $b > 0$ for a dilatant material and $b < 0$ for a contractant material. By setting $\beta = b = 0$, the J2 flow (von Mises) plasticity model is recovered, which is useful for modeling the undrained condition in a cohesive soil.

With the plastic potential function $\varphi(\boldsymbol{\sigma}, \boldsymbol{\alpha})$ defined in (54), the evolution of $\boldsymbol{\xi}$ then becomes

$$\dot{\boldsymbol{\xi}} = \lambda\frac{\partial\varphi}{\partial\boldsymbol{\alpha}} = \lambda\begin{Bmatrix}\sqrt{3}b\\ 1\end{Bmatrix}. \tag{56}$$

Note that b takes the form

$$b = \frac{\dot{v}^{\mathrm{p}}}{\sqrt{3\dot{e}^{\mathrm{p}}}} \tag{57}$$

which is analogous to the dilatancy factor used by Rudnicki and Rice [66] and Rudnicki [71].

6.2. Drucker–Prager plasticity model with strong discontinuity

Here, the standard non-associated Drucker–Prager plasticity model presented in the previous section is placed within the framework of Section 5. In particular, the two model-specific features which need to be derived are the localization condition and stress–displacement relation.

Recall the localization condition, which detects the presence of discontinuous displacements

$$\boldsymbol{A}\cdot\boldsymbol{m} = \mathbf{0}; \quad \boldsymbol{A} = \boldsymbol{n}\cdot\boldsymbol{C}^{\mathrm{ep}}\cdot\boldsymbol{n} \tag{58}$$

where for Drucker–Prager plasticity the elastic–perfectly plastic tangent modulus tensor is

$$\boldsymbol{C}^{\mathrm{ep}} = \left(\bar{K} - \frac{2\bar{\mu}}{3} - \frac{3\beta b\bar{K}^2}{\chi}\right)\mathbf{1}\otimes\mathbf{1} + 2\bar{\mu}\boldsymbol{I} - \frac{6\bar{\mu}^2}{\chi}\,\hat{\boldsymbol{n}}\otimes\hat{\boldsymbol{n}} - \frac{3\sqrt{2}\bar{\mu}\bar{K}}{\chi}\,(\beta\hat{\boldsymbol{n}}\otimes\mathbf{1} + b\mathbf{1}\otimes\hat{\boldsymbol{n}}), \tag{59}$$

where $\chi = 3(\bar{\mu} + \beta b\bar{K})$. Note that $\boldsymbol{C}^{\mathrm{ep}}$ is the same as the continuum elastic–plastic tangent modulus tensor $\boldsymbol{c}^{\mathrm{ep}}$ if $\mathscr{H}$ from (18) is added to χ in (59), where $\mathscr{H} = 3b^2K' + H'$. The corresponding elastic–perfectly plastic acoustic tensor is

$$\boldsymbol{A} = \boldsymbol{n}\cdot\boldsymbol{C}^{\mathrm{ep}}\cdot\boldsymbol{n} = \left(\bar{K} + \frac{\bar{\mu}}{3} - \frac{3\beta b\bar{K}^2}{\chi}\right)\boldsymbol{n}\otimes\boldsymbol{n} + \bar{\mu}\mathbf{1} - \frac{6\bar{\mu}^2}{\chi}\boldsymbol{N}\otimes\boldsymbol{N} - \frac{3\sqrt{2}\bar{\mu}\bar{K}}{\chi}\,(\beta\boldsymbol{N}\otimes\boldsymbol{n} + b\boldsymbol{n}\otimes\boldsymbol{N}), \tag{60}$$

where $\boldsymbol{N} = \hat{\boldsymbol{n}}\cdot\boldsymbol{n} = \boldsymbol{n}\cdot\hat{\boldsymbol{n}}$. Note that neither $\boldsymbol{C}^{\mathrm{ep}}$ nor $\boldsymbol{A}$ has major symmetry unless $\beta = b$.

The localization condition $\boldsymbol{A}\cdot\boldsymbol{m} = \mathbf{0}$ naturally yields the following form of the localization condition:

$$\boldsymbol{m}\cdot\boldsymbol{A}\cdot\boldsymbol{m} = 0 \tag{61}$$

which may be viewed as a loss of strong ellipticity of $\boldsymbol{C}^{\mathrm{ep}}$ [72]. Recall (38), which for Drucker–Prager plasticity yields

$$(\boldsymbol{m}\otimes\boldsymbol{n})^s = \Lambda\left(\sqrt{\frac{3}{2}}\,\hat{\boldsymbol{n}} + \frac{1}{\sqrt{3}}\,b\mathbf{1}\right) \tag{62}$$

and

$$\boldsymbol{m}\cdot\boldsymbol{n} = \Lambda\sqrt{3}b. \tag{63}$$

Expand $\boldsymbol{m}\cdot\boldsymbol{A}\cdot\boldsymbol{m} = 0$ as

$$\left(\bar{K} + \frac{\bar{\mu}}{3} - \frac{3\beta b\bar{K}^2}{\chi}\right)(\boldsymbol{m}\cdot\boldsymbol{n})^2 + \bar{\mu} - \frac{6\bar{\mu}^2}{\chi}\,(\hat{\boldsymbol{n}} : (\boldsymbol{m}\otimes\boldsymbol{n})^s)^2 - \frac{3\sqrt{2}\bar{\mu}\bar{K}}{\chi}\,(\beta + b)(\boldsymbol{m}\cdot\boldsymbol{n})\,(\hat{\boldsymbol{n}} : (\boldsymbol{m}\otimes\boldsymbol{n})^s) = 0. \tag{64}$$

Substituting Eqs. (62) and (63) into Eq. (64) yields a solution for Λ:

$$\Lambda = \pm\frac{1}{\sqrt{3 - b^2}}\,. \tag{65}$$

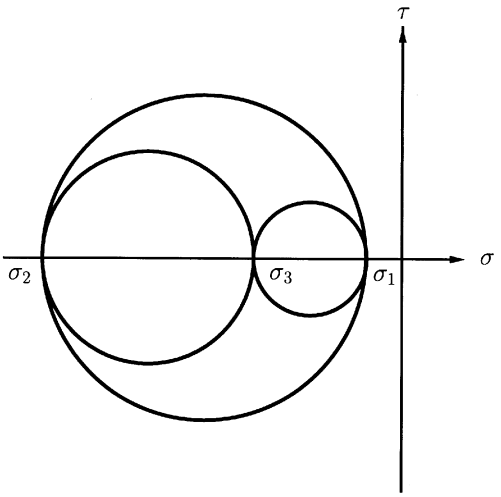

Fig. 3. Mohr circles for localization condition stress analysis in plane strain.

Recall that $\Lambda = \lambda_\delta/\dot{\zeta}$ where $\lambda_\delta > 0, \dot{\zeta} > 0$. Thus, the solution of interest is

$$\Lambda = \frac{1}{\sqrt{3 - b^2}}\,. \tag{66}$$

As a result of Eq. (66), the jump dilation angle ψ may be determined from the following equation:

$$\sin\psi = \boldsymbol{m}\cdot\boldsymbol{n} = \frac{\sqrt{3}b}{\sqrt{3 - b^2}}\,, \tag{67}$$

where b is determined from Eq. (57).

Consider a plane strain stress condition to calculate the localization condition and slip line orientation. Without loss of generality, the analysis is carried out in the principal stress space, where σ_2 is the minor principal stress (major compressive principal stress), σ_1 is the major principal stress, and σ_3 is the intermediate principal stress, such that $0 \geqslant \sigma_1 \geqslant \sigma_3 \geqslant \sigma_2$ and $|\sigma_1| \leqslant |\sigma_3| \leqslant |\sigma_2|$; refer to the Mohr circles in Fig. 3 (this ordering corresponds to a plane strain stress condition in terms of aligning the principal stresses with the coordinate axes, but is still general). Refer to Fig. 2 to construct the unit vectors

$$\boldsymbol{n} = \begin{Bmatrix} \cos\theta \\ \sin\theta \\ 0 \end{Bmatrix}, \quad \boldsymbol{m} = \begin{Bmatrix} \cos\eta \\ -\sin\eta \\ 0 \end{Bmatrix}, \quad \eta = 90^\circ - \theta - \psi. \tag{68}$$

Recall from Eq. (62) the expression for the symmetric tensor product of $\boldsymbol{m}$ and $\boldsymbol{n}$, written now explicitly as

$$\begin{bmatrix} \cos\eta\cos\theta & \cos\eta\sin\theta & 0 \\ -\sin\eta\cos\theta & -\sin\eta\sin\theta & 0 \\ 0 & 0 & 0 \end{bmatrix}^s$$

$$= \frac{1}{\sqrt{3-b^2}} \begin{bmatrix} \sqrt{\frac{3}{2}}\hat{n}_1 + \frac{1}{\sqrt{3}}b & 0 & 0 \\ 0 & \sqrt{\frac{3}{2}}\hat{n}_2 + \frac{1}{\sqrt{3}}b & 0 \\ 0 & 0 & \sqrt{\frac{3}{2}}\hat{n}_3 + \frac{1}{\sqrt{3}}b \end{bmatrix}. \tag{69}$$

For $(\boldsymbol{m}\otimes\boldsymbol{n})^s$ to diagonalize, the following must hold

$$\cos\eta\sin\theta - \sin\eta\cos\theta = \sin(\theta-\eta) = 0 \tag{70}$$

or

$$\theta - \eta = 2\theta - 90^\circ + \psi = 0 \tag{71}$$

which implies

$$\boxed{\theta = \pm(45^\circ - \psi/2)}\,, \tag{72}$$

where the $\pm$ comes from Fig. 2. Thus, (72) is the orientation of the normal to the slip line with respect to the major principal stress axis (see Fig. 2). This result has also been reached by Roscoe ([73], p. 166) and Atkinson ([74], p. 217) and refuted by Vardoulakis et al. [3]. For deviatoric plastic flow, $b = 0 \Rightarrow \psi = 0$, and the orientation $\theta = 45^\circ$ is recovered.

To obtain a condition on the stress state at which localization is detected, take the difference between the (1,1) and (2,2) components of (69), which yields

$$\cos\eta\cos\theta + \sin\eta\sin\theta = \sqrt{\frac{3}{3-b^2}}\,\frac{(s_1 - s_2)/\sqrt{2}}{\|\boldsymbol{s}\|}\,, \tag{73}$$

where

$$\cos\eta\cos\theta + \sin\eta\sin\theta = \cos^2\theta + \sin^2\theta = 1. \tag{74}$$

Thus, the localization condition may be expressed in terms of a deviator stress ratio h defined as

$$\boxed{h := \frac{\|\boldsymbol{s}\|}{\sqrt{2}r} = \sqrt{\frac{3}{3-b^2}}}\,, \tag{75}$$

where $r = (s_1 - s_2)/2 = (\sigma_1 - \sigma_2)/2$. A straightforward analysis determines the range of h as [53]

$$\boxed{1 \leqslant h \leqslant \frac{2}{\sqrt{3}}} \tag{76}$$

which defines the range of the deviator stress ratio h in the localization condition (75).

The stress–displacement relation governs the evolution of plastic softening localized to the discontinuity $\mathscr{S}$. Upon the detection of discontinuous displacement fields via the localization condition, the plastic flow is localized to the discontinuity via $\lambda = \lambda_\delta \delta_\mathscr{S}$; likewise, softening is localized to the discontinuity via $\boldsymbol{H}^{-1} = \boldsymbol{H}_\delta^{-1} \delta_\mathscr{S}$. Thus, the stress–displacement relation becomes the constitutive equation for post-localization plasticity. The standard plasticity equations no longer apply, except to provide the framework in which the strong discontinuity is incorporated to produce the bifurcated solution.

Recall the general form for the stress displacement relation from (41):

$$\dot{\zeta} = \frac{\mathrm{tr}(\partial_{\boldsymbol{\sigma}} \varphi)}{\mathscr{H}_\delta \boldsymbol{m} \cdot \boldsymbol{n}} \, \partial_{\boldsymbol{\sigma}} \phi : \dot{\boldsymbol{\sigma}} = \frac{1}{\mathscr{H}_\delta \Lambda} \, \partial_{\boldsymbol{\sigma}} \phi : \dot{\boldsymbol{\sigma}}, \tag{77}$$

where $\mathscr{H}_\delta = 3b^2 K_\delta + H_\delta$,

$$\boldsymbol{H}_\delta = \begin{bmatrix} K_\delta & 0 \\ 0 & H_\delta \end{bmatrix} \tag{78}$$

and $\Lambda = (3 - b^2)^{-1/2}$. The rate form of the stress–displacement relation is then found to be [53]

$$\dot{q} + \frac{\sqrt{3}\beta}{\sqrt{3 - b^2}} \, \dot{p} = \frac{\mathscr{H}_\delta}{3 - b^2} \, \dot{\zeta}, \tag{79}$$

where $q := \boldsymbol{m} \cdot \boldsymbol{s} \cdot \boldsymbol{n}$. Integrate (79) to yield the resolved stress at time instant t, $Q(t)$, as

$$\begin{aligned} Q(t) &:= q(t) + \frac{\sqrt{3}\beta}{\sqrt{3 - b^2}} \, p(t) \\ &= q(0) + \frac{\sqrt{3}\beta}{\sqrt{3 - b^2}} \, p(0) + \frac{\mathscr{H}_\delta}{3 - b^2} \, \zeta(t), \end{aligned} \tag{80}$$

where $t = 0$ corresponds to the onset of localization and $\zeta(0) = 0$ (i.e., there is no jump displacement yet developed at the instant of localization).

7. Finite element implementation

The assumed enhanced strain (AES) method [75] is a logical choice as a variational framework for implementing the strong discontinuity approach because it satisfies the two conditions necessary and sufficient for convergence when an enhanced strain field is introduced: (1) stability, and (2) consistency (i.e. the patch test); these two conditions will be described later.

7.1. Variational form of AES method

The AES method for the linearized theory stems from an additive decomposition of the infinitesimal strain tensor into compatible and enhanced parts:

$$\boldsymbol{\varepsilon} = \underbrace{\boldsymbol{\nabla}^s \boldsymbol{u}}_{\text{compatible}} + \underbrace{\tilde{\boldsymbol{\varepsilon}}}_{\text{enhanced}}, \tag{81}$$

where the enhanced strain field may be derived from incompatible displacement fields across element sides. Introducing the newly defined strain field (81) into an energy functional Π and applying the stationary condition ($\delta\Pi = 0$) yields the modified three-field variational form [75]:

$$\int_\Omega \boldsymbol{\nabla}^s(\delta\boldsymbol{u}) : \boldsymbol{\sigma}\, \mathrm{d}\Omega = \int_\Omega \delta\boldsymbol{u}\cdot\boldsymbol{b}\, \mathrm{d}\Omega + \int_{\partial_t\Omega} \delta\boldsymbol{u}\cdot\boldsymbol{t}\, \mathrm{d}\Gamma, \tag{82}$$

$$\int_\Omega \delta\boldsymbol{\sigma} : \tilde{\boldsymbol{\varepsilon}}\, \mathrm{d}\Omega = 0, \tag{83}$$

$$\int_\Omega \delta\tilde{\boldsymbol{\varepsilon}} : (-\boldsymbol{\sigma} + \partial_{\varepsilon}\Psi)\, \mathrm{d}\Omega = 0. \tag{84}$$

Because of the orthogonality condition on the stress and enhanced strain spaces in (83), the stress field is eliminated from the variational equations and (84) drops out.

Since the purpose of the enhanced strain field is to 'enhance' the compatible strain field, it makes sense that their spaces have null intersection:

$$\tilde{\mathscr{E}} \cap \mathscr{E} = \emptyset \tag{85}$$

where the space for the compatible strains is

$$\mathscr{E} = \{\boldsymbol{\varepsilon} : \Omega \to \mathbb{S};\ \boldsymbol{\varepsilon} = \boldsymbol{\nabla}^s \boldsymbol{u}\} \tag{86}$$

and the space for the enhanced strains is

$$\tilde{\mathscr{E}} = \{\tilde{\boldsymbol{\varepsilon}} : \Omega \to \mathbb{S};\ \tilde{\boldsymbol{\varepsilon}} \text{ is assumed}\}. \tag{87}$$

It has been shown for the discrete problem that (85) leads to stability of the AES method [75].

For the patch test to be satisfied — as revisited in Taylor et al. [76] — piecewise constant stress functions must be admissible. This condition will directly affect the choice of the discrete enhanced strain variation $\delta\tilde{\boldsymbol{\varepsilon}}^h$. Rewrite (83) as

$$\int_\Omega \boldsymbol{\sigma} : \delta\tilde{\boldsymbol{\varepsilon}}\, \mathrm{d}\Omega = 0 \tag{88}$$

because the *spaces* are orthogonal. Thus, piecewise constant stress functions $\boldsymbol{\sigma}_0$ will require

$$\int_\Omega \delta\tilde{\boldsymbol{\varepsilon}}\, \mathrm{d}\Omega = \mathbf{0} \tag{89}$$

which will be described in particular for singular enhanced strains.

7.2. Reparameterization of the displacement field

The need for a reparameterized displacement field was recognized by Simo et al. [43] for the 1D problem. The motivation stems from the fact that the nodal displacements are the total displacements and thus already contain the effect of the displacement jump within the element. The idea then is to confine the enhancement within the element boundaries. The resulting reparameterization for the general three-dimensional problem is as follows:

$$\boldsymbol{u}^h(\boldsymbol{x}, t) = \bar{\boldsymbol{u}}^h(\boldsymbol{x}, t) + [\![\boldsymbol{u}^h(t)]\!] M_{\mathscr{S}}(\boldsymbol{x}). \tag{90}$$

The restrictions on this function $M_{\mathscr{S}}(\boldsymbol{x}) : \bar{\Omega}^e_{\text{loc}} \to \mathbb{R}$ are

1. compact support in $\bar{\Omega}^h$; i.e. $M_{\mathscr{S}}(\boldsymbol{x}) = 0$ for $\boldsymbol{x}$ outside of $\bar{\Omega}^h$ and $\boldsymbol{x} \in \partial\Omega^h$, where $\bar{\Omega}^h = \Omega^h \cup \partial\Omega^h$;
2. $[\![M_{\mathscr{S}}]\!] = 1$ at $\mathscr{S}$.

Thus, the construction of $M_{\mathscr{S}}(\boldsymbol{x})$ is as follows:

$$M_{\mathscr{S}}(\boldsymbol{x}) = H_{\mathscr{S}}(\boldsymbol{x}) - f^h(\boldsymbol{x}), \tag{91}$$

where

$$f^h(\boldsymbol{x}) = \begin{cases} 1 & \text{at node } A \in \partial\Omega^h_+, \\ 0 & \text{at note } A \in \partial\Omega^h_-. \end{cases} \tag{92}$$

Recall that the unit normal $\boldsymbol{n}$ to the discontinuity $\mathscr{S}$ points into Ω^h_+.

For the two-dimensional problem, it is possible to formulate these functions $M_{\mathscr{S}}$ for the two slip line cases for a quadrilateral element as shown in Fig. 4. The functions which result via the above

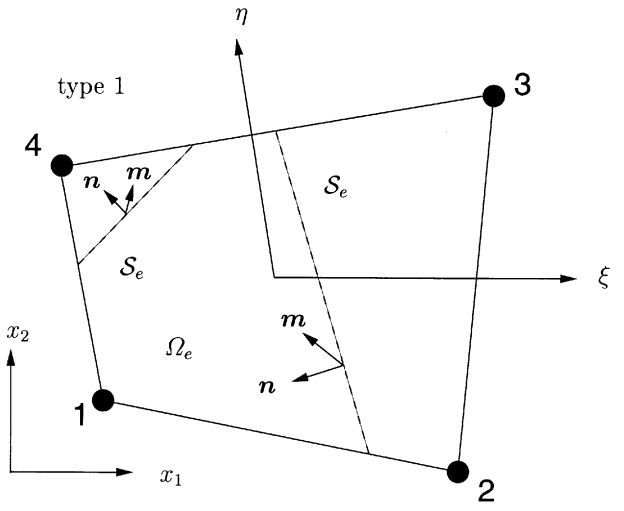

Fig. 4. Two slip line types in a quadrilateral element.

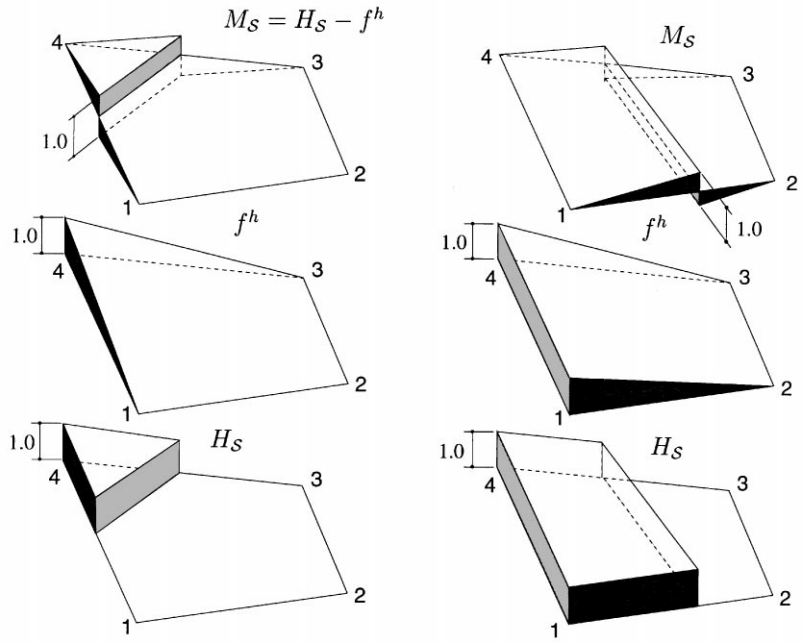

Fig. 5. Slip line types 1 and 2. Motivation for enhanced strain interpolations via $M_{\mathscr{S}}$.

construction are shown in Fig. 5. The function f^h for slip line type 1 in Fig. 5 is the shape function at that node (node 4 in Fig. 5), and f^h for type 2 is the sum of the shape functions at nodes and 4.

With the displacement field now reparameterized and the variational form of the AES method in place, it is possible to proceed with formulating the nonlinear matrix finite element equations. A thorough analysis of the weak form with strong discontinuity has been presented by Simo and Oliver [44].

7.3. Variational equations

Let $\bar{\Omega}^h = \cup_{e=1}^{n_{\text{el}}} \bar{\Omega}_e^h$ be the finite element discretization of a closed region $\bar{\Omega}$, and $\bar{\Omega}_{\text{loc}}^h = \cup_{e=1}^{n_{\text{el, loc}}} \bar{\Omega}_{\text{loc},e}^h$ be the finite element discretization of the localized region, where $\bar{\Omega}_{\text{loc}}^h \subset \bar{\Omega}^h$, n_{el} is the number of elements, and $n_{\text{el,loc}}$ is the number of localized elements which is not a priori known. The resulting discretized weak form results as follows [44]:

$$\int_{\Omega^h} \nabla^s \bar{\boldsymbol{\eta}}^h : \boldsymbol{\sigma}^h \, \mathrm{d}\Omega = \int_{\Omega^h} \bar{\boldsymbol{\eta}}^h \cdot \boldsymbol{b}^h \, \mathrm{d}\Omega + \int_{\partial_t \Omega^h} \bar{\boldsymbol{\eta}}^h \cdot \boldsymbol{t}^h \, \mathrm{d}\Gamma,$$

$$\int_{\Omega_{\text{loc},e}^h} \tilde{\boldsymbol{\gamma}}^h : \boldsymbol{\sigma}^h \, \mathrm{d}\Omega = 0, \tag{93}$$

where $\bar{\boldsymbol{\eta}} = \delta \bar{\boldsymbol{u}}$ and $\tilde{\boldsymbol{\gamma}} = \delta \tilde{\boldsymbol{\varepsilon}}$.

The rest of this presentation will concentrate on the formulation for an element e with strong discontinuity. Recall the reparameterized displacement field written for element e as

$$\boldsymbol{u}_e^h = \bar{\boldsymbol{u}}_e^h + [\![\boldsymbol{u}_e^h]\!] M_{\mathscr{S}_e}^h, \quad [\![\boldsymbol{u}_e^h]\!] = \zeta_e^h \boldsymbol{m}_e, \tag{94}$$

where now

$$\boldsymbol{\eta}_e^h = \delta \boldsymbol{u}_e^h = \bar{\boldsymbol{\eta}}_e^h + [\![\boldsymbol{\eta}_e^h]\!] M_{\mathscr{S}_e}^h, \quad [\![\boldsymbol{\eta}_e^h]\!] = \eta_e^h \boldsymbol{m}_e \tag{95}$$

and

$$M_{\mathscr{S}_e}^h = H_{\mathscr{S}_e} - f_e^h \tag{96}$$

with f_e^h defined in Fig. 5. Thus, the strain and strain variations become

$$\boldsymbol{\varepsilon}_e^h := \boldsymbol{\nabla}^s \boldsymbol{u}_e^h = \boldsymbol{\nabla}^s \bar{\boldsymbol{u}}_e^h + \tilde{\boldsymbol{\varepsilon}}_e^h, \tag{97}$$

where

$$\tilde{\boldsymbol{\varepsilon}}_e^h = -\zeta_e^h (\boldsymbol{m}_e \otimes \boldsymbol{\nabla} f_e^h)^s + \zeta_e^h (\boldsymbol{m}_e \otimes \boldsymbol{n}_e)^s \delta_{\mathscr{S}_e} \tag{98}$$

and

$$\gamma_e^h := \boldsymbol{\nabla}^s \boldsymbol{\eta}_e^h = \boldsymbol{\nabla}^s \bar{\boldsymbol{\eta}}_e^h + \tilde{\gamma}_e^h. \tag{99}$$

Recall that the choice of $\tilde{\gamma}_e^h$ is made such that $(93)_2$ is satisfied for piecewise constant stress fields $\boldsymbol{\sigma}_0^h$, or

$$\int_{\Omega_{\mathrm{loc},e}^h} \tilde{\gamma}_e^h \, \mathrm{d}\Omega = \boldsymbol{0}. \tag{100}$$

Eq. (100) may be written independently of other localized elements because the enhanced strains are discontinuous between elements (which is also a property of the standard C^0 finite element theory, that strains are typically discontinuous between elements; the C^0 theory, however, requires continuous displacements, which is not a requirement of the functions $M_{\mathscr{S}}$ which motivate the enhanced strains used in the AES method). Considering (100), choose $\tilde{\gamma}_e^h$ to have the following form [45]:

$$\tilde{\gamma}_e^h = -\eta_e^h \frac{l_{\mathscr{S}_e}}{A_e} (\boldsymbol{m}_e \otimes \boldsymbol{n}_e)^s + \eta_e^h (\boldsymbol{m}_e \otimes \boldsymbol{n}_e)^s \delta_{\mathscr{S}_e}, \tag{101}$$

where $l_{\mathscr{S}_e}$ is the length of the slip line within element e, and A_e is the area of element e. Thus, satisfaction of the patch test is ensured.

7.4. Matrix finite element equations

The standard finite element interpolations in isoparametric coordinates $\boldsymbol{\xi}$ are as follows:

$$\bar{\boldsymbol{u}}_e^h(\boldsymbol{\xi}) = \sum_{A=1}^{n_{\mathrm{nds}}} N^A(\boldsymbol{\xi}) \boldsymbol{d}_e^A; \quad \bar{\boldsymbol{\eta}}_e^h = \sum_{A=1}^{n_{\mathrm{nds}}} N^A(\boldsymbol{\xi}) \boldsymbol{c}_e^A \tag{102}$$

where n_{nds} is the number of nodes of an element e, $N^A(\boldsymbol{\xi})$ is the shape function at node A, and $\boldsymbol{d}_e^A$ and $\boldsymbol{c}_e^A$ are the displacement vector and displacement variation vector, respectively, at node A. It is convenient to write the expressions in (102) in the following matrix form:

$$\bar{\boldsymbol{u}}_e^h(\boldsymbol{\xi}) = \boldsymbol{N}_e(\boldsymbol{\xi})\cdot\boldsymbol{d}_e, \qquad \bar{\boldsymbol{\eta}}_e^h = \boldsymbol{N}_e(\boldsymbol{\xi})\cdot\boldsymbol{c}_e, \tag{103}$$

where $\boldsymbol{N}_e(\boldsymbol{\xi})$ is the element shape function matrix, and $\boldsymbol{d}_e$ and $\boldsymbol{c}_e$ are the displacement vector and displacement variation vector, respectively, for element e. Taking the symmetric gradient of the expressions in (103) yields

$$\boldsymbol{\nabla}^s\bar{\boldsymbol{u}}_e^h(\boldsymbol{\xi}) = \boldsymbol{B}_e(\boldsymbol{\xi})\cdot\boldsymbol{d}_e, \qquad \boldsymbol{\nabla}^s\bar{\boldsymbol{\eta}}_e^h = \boldsymbol{B}_e(\boldsymbol{\xi})\cdot\boldsymbol{c}_e, \tag{104}$$

where $\boldsymbol{B}_e(\boldsymbol{\xi})$ is the element strain–displacement matrix. Likewise, write $\tilde{\boldsymbol{\varepsilon}}_e^h$ and $\tilde{\boldsymbol{\gamma}}_e^h$ in matrix form as

$$\tilde{\boldsymbol{\varepsilon}}_e^h = -\boldsymbol{G}_e\zeta_e^h + \boldsymbol{F}_e\zeta_e^h\delta_{\mathscr{S}_e}, \quad \boldsymbol{G}_e = [(\boldsymbol{m}_e\otimes\boldsymbol{\nabla}f_e^h)^s] \tag{105}$$

and

$$\tilde{\boldsymbol{\gamma}}_e^h = -\frac{l_{\mathscr{S}_e}}{A_e}\boldsymbol{F}_e\eta_e^h + \boldsymbol{F}_e\eta_e^h\delta_{\mathscr{S}_e}, \quad \boldsymbol{F}_e = [(\boldsymbol{m}_e\otimes\boldsymbol{n}_e)^s] \tag{106}$$

where $[\bullet]$ denotes matrix form of the tensor. Substituting the matrix expressions for $\bar{\boldsymbol{\eta}}_e^h$ from (103), $\boldsymbol{\nabla}^s\bar{\boldsymbol{\eta}}_e^h$ from Eq. (104), and $\tilde{\boldsymbol{\gamma}}_e^h$ from Eq. (106) into Eq. (93), and assuming arbitrary values of $\boldsymbol{c}_e$ and η_e^h, the nonlinear finite element equations expressed in residual form result as

$$\begin{aligned}
\boldsymbol{r}_e &:= \int_{\Omega_e^h}\boldsymbol{B}_e^{\mathrm{T}}\boldsymbol{\sigma}^h\,\mathrm{d}\Omega - \int_{\Omega_e^h}\boldsymbol{N}_e^{\mathrm{T}}\boldsymbol{b}^h\,\mathrm{d}\Omega - \int_{\partial_t\Omega_e^h}\boldsymbol{N}_e^{\mathrm{T}}\boldsymbol{t}^h\,\mathrm{d}\Gamma = \boldsymbol{0},\\
b_e &:= \frac{1}{A_e}\int_{\Omega_{\text{loc},e}^h}\boldsymbol{F}_e^T\boldsymbol{\sigma}^h\,\mathrm{d}\Omega - (q_{\mathscr{S}_e}^h + \boldsymbol{n}_e\cdot\boldsymbol{m}_e p_{\mathscr{S}_e}^h) = 0,
\end{aligned} \tag{107}$$

where $\boldsymbol{r}_e$ is the standard residual for equilibrium within an element e, b_e is the residual expressing equilibrium along the discontinuity $\mathscr{S}_e$, $\boldsymbol{\sigma}^h$ is in vector form, and $\boldsymbol{n}_e\cdot\boldsymbol{m}_e = \sqrt{3}b/\sqrt{3-b^2}$. Note that Eq. $(107)_2$ imposes the following conditions:

$$q_{\mathscr{S}_e}^h = \frac{1}{A_e}\int_{\Omega_{\text{loc},e}^h}\boldsymbol{m}_e\cdot\boldsymbol{s}^h\cdot\boldsymbol{n}_e\,\mathrm{d}\Omega \tag{108}$$

and

$$p_{\mathscr{S}_e}^h = \frac{1}{3A_e}\int_{\Omega_{\text{loc},e}^h}\mathrm{tr}(\boldsymbol{\sigma}^h)\,\mathrm{d}\Omega \tag{109}$$

for the resolved stress values along the discontinuity $\mathscr{S}_e$. Consider $(107)_2$ more closely, and recall the integrated form of the stress–displacement relation from (80):

$$q_{\mathscr{S}_e}^h + \frac{\sqrt{3}\beta}{\sqrt{3-b^2}}p_{\mathscr{S}_e}^h = q_{\mathscr{S}_e,\text{loc}}^h + \frac{\sqrt{3}\beta}{\sqrt{3-b^2}}p_{\mathscr{S}_e,\text{loc}}^h + \frac{\mathscr{H}_\delta}{3-b^2}\zeta_e^h, \tag{110}$$

where the subscript $(\bullet)_{,\mathrm{loc}}$ designates the resolved stress value at onset of localization. Rewrite Eq. (110) for $q^h_{\mathscr{S}_e}$ as

$$q^h_{\mathscr{S}_e} = -\frac{\sqrt{3}\beta}{\sqrt{3-b^2}}\, p^h_{\mathscr{S}_e} + q^h_{\mathscr{S}_e,\mathrm{loc}} + \frac{\sqrt{3}\beta}{\sqrt{3-b^2}}\, p^h_{\mathscr{S}_e,\mathrm{loc}} + \frac{\mathscr{H}_\delta}{3-b^2}\, \zeta^h_e. \tag{111}$$

Substituting (111) into $(107)_2$ and using (109) yields

$$b_e = \frac{1}{A_e}\int_{\Omega^h_{\mathrm{loc},e}} \boldsymbol{F}_e^{\mathrm{T}}\hat{\boldsymbol{\sigma}}^h \,\mathrm{d}\Omega - \left(q^h_{\mathscr{S}_e,\mathrm{loc}} + \frac{\sqrt{3}\beta}{\sqrt{3-b^2}}\, p^h_{\mathscr{S}_e,\mathrm{loc}} + \frac{\mathscr{H}_\delta}{3-b^2}\, \zeta^h_e\right) = 0 \tag{112}$$

where

$$\hat{\boldsymbol{\sigma}}^h = \boldsymbol{s}^h + \frac{\beta}{3b}\,\mathrm{tr}(\boldsymbol{\sigma}^h)\{\mathbf{1}\}, \tag{113}$$

and $\{\mathbf{1}\}$ is the vector form of $\mathbf{1}$. Thus, when linearizing the residual b_e, this new form in Eq. (112) must be used.

Recall that the stress $\boldsymbol{\sigma}^h$ is regular, but with a reparameterization of the displacement field in Eq. (94), the stress rate becomes

$$\dot{\boldsymbol{\sigma}}^h = \boldsymbol{D}^{\mathrm{e}} \cdot [\dot{\bar{\boldsymbol{\varepsilon}}}^h_e - \boldsymbol{G}_e \dot{\zeta}^h_e] \quad \text{in } \Omega^h_{\mathrm{loc},e}/\mathscr{S}_e \tag{114}$$

where $\boldsymbol{D}^{\mathrm{e}}$ is the matrix form of $\boldsymbol{c}^{\mathrm{e}}$ and $\dot{\bar{\boldsymbol{\varepsilon}}}^h_e = \boldsymbol{\nabla}^s \dot{\boldsymbol{u}}^h_e$. For subsequent derivations, the discretization flag h is left off for certain terms for ease of presentation. Integrating Eq. (114) yields

$$\boldsymbol{\sigma}_{n+1} = \boldsymbol{\sigma}^{\mathrm{tr}}_{n+1} - \boldsymbol{D}^{\mathrm{e}} \cdot \boldsymbol{G}_e \Delta\zeta_e \quad \text{in } \Omega^h_{\mathrm{loc},e}/\mathscr{S}_e \tag{115}$$

where $\boldsymbol{\sigma}^{\mathrm{tr}}_{n+1} = \boldsymbol{\sigma}_n + \boldsymbol{D}^{\mathrm{e}} \cdot \Delta\bar{\boldsymbol{\varepsilon}}_e$ is the trial stress, $\Delta\bar{\boldsymbol{\varepsilon}}_e = \bar{\boldsymbol{\varepsilon}}_{e,n+1} - \bar{\boldsymbol{\varepsilon}}_{e,n}$, $\Delta\zeta_e = \zeta_{e,n+1} - \zeta_{e,n}$, and $n+1$ is the current time step. Integrating the stress–displacement relation in Eq. (79) yields

$$|q_{\mathscr{S}_e,n+1}| + \frac{\sqrt{3}\beta}{\sqrt{3-b^2}}\, p_{\mathscr{S}_e,n+1} = |q_{\mathscr{S}_e,\mathrm{loc}}| + \frac{\sqrt{3}\beta}{\sqrt{3-b^2}}\, p_{\mathscr{S}_e,\mathrm{loc}} + \frac{\mathscr{H}_\delta}{3-b^2}\, |\zeta_{e,n+1}| \quad \text{on } \mathscr{S}_e \tag{116}$$

where $\mathscr{H}_\delta < 0$, and $\mathscr{H}_\delta$ is constant for linear softening along the discontinuity. Note that if one were to change the sign convention from continuum mechanics convention ($\varepsilon > 0$ and $\sigma > 0$ in tension for 1D) to soil mechanics convention ($\varepsilon > 0$ and $\sigma > 0$ in compression), Eq. (116) would still be valid taking account of the appropriate change in sign before the pressure term in the yield function in Eq. (49). Thus, the stress update for a localized element e is fully defined by Eq. (115) and (116).

Linearization of the (in general) nonlinear finite element equations in Eq. (107) for solution by the Newton–Raphson method (refer to Simo and Hughes [61]) yields

$$\begin{aligned} -\boldsymbol{r}^k_{e,n+1} &= \boldsymbol{K}^{\mathrm{e}}_{dd} \cdot \Delta\boldsymbol{d}_e + \boldsymbol{K}^{\mathrm{e}}_{d\zeta}\Delta\zeta_e \\ -b^k_{e,n+1} &= (\boldsymbol{K}^{\mathrm{e}}_{\zeta d} + \boldsymbol{K}^{\mathrm{e}}_{d}) \cdot \Delta\boldsymbol{d}_e + (K^{\mathrm{e}}_{\zeta\zeta} + K^{\mathrm{e}}_{\zeta})\Delta\zeta_e \end{aligned} \tag{117}$$

where

$$\boldsymbol{K}^{\mathrm{e}}_{dd} = \int_{\Omega^h_e} \boldsymbol{B}^{\mathrm{T}}_e \frac{\partial \boldsymbol{\sigma}^k_{n+1}}{\partial \boldsymbol{\varepsilon}^k_{n+1}} \boldsymbol{B}_e \, \mathrm{d}\Omega$$

$$\boldsymbol{K}^{\mathrm{e}}_{d\zeta} = -\int_{\Omega^h_e} \boldsymbol{B}^{\mathrm{T}}_e \frac{\partial \boldsymbol{\sigma}^k_{+1}}{\partial \boldsymbol{\varepsilon}^k_{n+1}} \boldsymbol{G}_e \, \mathrm{d}\Omega$$

$$\boldsymbol{K}^{\mathrm{e}}_{\zeta d} = \frac{1}{A_e} \int_{\Omega^h_{e,\mathrm{loc}}} \boldsymbol{F}^{\mathrm{T}}_e \frac{\partial \hat{\boldsymbol{\sigma}}^k_{n+1}}{\partial \boldsymbol{\varepsilon}^k_{n+1}} \boldsymbol{B}_e \, \mathrm{d}\Omega$$

$$\boldsymbol{K}^{\mathrm{e}}_{d} = -\boldsymbol{K}^{\mathrm{e}}_{\zeta d} \text{ (for elastic unloading)}$$

$$K^{\mathrm{e}}_{\zeta\zeta} = -\frac{1}{A_e} \int_{\Omega^h_{e,\mathrm{loc}}} \boldsymbol{F}^{\mathrm{T}}_e \frac{\partial \hat{\boldsymbol{\sigma}}^k_{n+1}}{\partial \boldsymbol{\varepsilon}^k_{n+1}} \boldsymbol{G}_e \, \mathrm{d}\Omega$$

$$K^{\mathrm{e}}_{\zeta} = -\frac{\mathscr{H}_\delta}{3 - b^2} \tag{118}$$

and $k+1$ is the current iteration. Since the strain due to the jump displacement is treated as an enhanced strain (see (98)), the jump displacement ζ_e may be assumed discontinuous between elements and thus may be condensed out of the equations at the element level to form the reduced system

$$\begin{aligned} -\tilde{\boldsymbol{r}}^k_{e,n+1} &= \tilde{\boldsymbol{K}}^{\mathrm{e}}_{dd} \cdot \Delta \boldsymbol{d}_e, \\ \tilde{\boldsymbol{r}}^k_{e,n+1} &= \boldsymbol{r}^k_{e,n+1} - \boldsymbol{K}^{\mathrm{e}}_{d\zeta} (K^{\mathrm{e}}_{\zeta\zeta} + K^{\mathrm{e}}_{\zeta})^{-1} b^k_{e,n+1}, \\ \tilde{\boldsymbol{K}}^{\mathrm{e}}_{dd} &= \boldsymbol{K}^{\mathrm{e}}_{dd} - \boldsymbol{K}^{\mathrm{e}}_{d\zeta} (K^{\mathrm{e}}_{\zeta\zeta} + K^{\mathrm{e}}_{\zeta})^{-1} (\boldsymbol{K}^{\mathrm{e}}_{\zeta d} + \boldsymbol{K}^{\mathrm{e}}_{d}). \end{aligned} \tag{119}$$

From (115) and (113) it is possible to derive the tangential moduli tensors as

$$\frac{\partial \boldsymbol{\sigma}^k_{n+1}}{\partial \boldsymbol{\varepsilon}^k_{n+1}} = \boldsymbol{D}^{\mathrm{e}}, \quad \frac{\partial \hat{\boldsymbol{\sigma}}^k_{n+1}}{\partial \boldsymbol{\varepsilon}^k_{n+1}} = \hat{\boldsymbol{D}}^{\mathrm{e}} \tag{120}$$

where $\boldsymbol{D}^{\mathrm{e}}$ and $\hat{\boldsymbol{D}}^{\mathrm{e}}$ are the matrix forms of $\boldsymbol{c}^{\mathrm{e}}$ and $\hat{\boldsymbol{c}}^{\mathrm{e}}$, respectively:

$$\begin{aligned} \boldsymbol{c}^{\mathrm{e}} &= \bar{K}\mathbf{1}\otimes\mathbf{1} + 2\bar{\mu}(\boldsymbol{I} - \tfrac{1}{3}\mathbf{1}\otimes\mathbf{1}), \\ \hat{\boldsymbol{c}}^{\mathrm{e}} &= \tfrac{\beta}{b}\bar{K}\mathbf{1}\otimes\mathbf{1} + 2\bar{\mu}(\boldsymbol{I} - \tfrac{1}{3}\mathbf{1}\otimes\mathbf{1}). \end{aligned} \tag{121}$$

For plastic loading,

$$\boldsymbol{K}^{\mathrm{e}}_{d} = \mathbf{0}, \quad K^{\mathrm{e}}_{\zeta} = -\frac{\mathscr{H}_\delta}{3 - b^2} \tag{122}$$

else for elastic unloading,

$$\begin{aligned} \boldsymbol{K}^{\mathrm{e}}_{d} &= -\boldsymbol{K}^{\mathrm{e}}_{\zeta d}, \\ K^{\mathrm{e}}_{\zeta} &= 0, \\ \tilde{\boldsymbol{K}}^{\mathrm{e}}_{dd} &= \boldsymbol{K}^{\mathrm{e}}_{dd}. \end{aligned} \tag{123}$$

The stress integration algorithm along the discontinuity in a localized element with linear softening is summarized as follows:

1. Compute the trial state by freezing localized plastic flow (i.e. use $\zeta_{e,n}$) and incrementing the total strain:

$$\boldsymbol{\sigma}_{n+1}^{\mathrm{tr},(k+1)} = \sigma_n + \boldsymbol{c}^{\mathrm{e}} : (\bar{\boldsymbol{\varepsilon}}_{n+1}^{k+1} - \bar{\boldsymbol{\varepsilon}}_n)$$

$$p_{n+1}^{\mathrm{tr},(k+1)} = \frac{1}{3}\,\mathrm{tr}(\boldsymbol{\sigma}_{n+1}^{\mathrm{tr},(k+1)})$$

$$\boldsymbol{s}_{n+1}^{\mathrm{tr},(k+1)} = \boldsymbol{\sigma}_{n+1}^{\mathrm{tr},(k+1)} - p_{n+1}^{\mathrm{tr},(k+1)}\mathbf{1}$$

$$q_{\mathscr{S}_e,n+1}^{\mathrm{tr},(k+1)} = \frac{1}{A_e}\int_{\Omega_{\mathrm{loc},e}^h} \boldsymbol{m}_e \cdot \boldsymbol{s}_{n+1}^{\mathrm{tr},(k+1)} \cdot \boldsymbol{n}_e \,\mathrm{d}\Omega$$

$$p_{\mathscr{S}_e,n+1}^{\mathrm{tr},(k+1)} = \frac{1}{3A_e}\int_{\Omega_{\mathrm{loc},e}^h} \mathrm{tr}(\boldsymbol{\sigma}_{n+1}^{\mathrm{tr},(k+1)})\,\mathrm{d}\Omega$$

$$Q_{\mathscr{S}_e}^{\mathrm{tr}} = \left(|q_{\mathscr{S}_e,n+1}^{\mathrm{tr},(k+1)}| + \frac{\sqrt{3}\beta}{\sqrt{3-b^2}}\, p_{\mathscr{S}_e,n+1}^{\mathrm{tr},(k+1)}\right) - \left(|q_{\mathscr{S}e,\mathrm{loc}}| + \frac{\sqrt{3}\beta}{\sqrt{-b^2}}\, p_{\mathscr{S}e,\mathrm{loc}} + \frac{\mathscr{H}_\delta}{3-b^2}\,|\zeta_{e,n}|\right). \tag{124}$$

2. Check for yielding along the discontinuity $\mathscr{S}_e$, and if yielding is detected, update stress:

IF $(Q_{\mathscr{S}_e}^{\mathrm{tr}} > 0)$ THEN

$$|q_{\mathscr{S}_e,n+1}^{k+1}| + \frac{\sqrt{3}\beta}{\sqrt{3-b^2}}\, p_{\mathscr{S}_e,n+1}^{k+1} = |q_{\mathscr{S}_e,\mathrm{loc}}| + \frac{\sqrt{3}\beta}{\sqrt{3-b^2}}\, p_{\mathscr{S}_e,\mathrm{loc}} + \frac{\mathscr{H}_\delta}{3-b^2}|\zeta_{e,n+1}^{k+1}|$$

$$\boldsymbol{K}_d^{\mathrm{e}} = \mathbf{0}$$

$$K_\zeta^{\mathrm{e}} = -\,\mathrm{sign}(q_{\mathscr{S}e,n+1}^{\mathrm{tr},(k+1)})\mathrm{sign}(\zeta_{e,n+1}^{k+1})\,\frac{\mathscr{H}_\delta}{3-b^2}$$

ELSE

$$q_{\mathscr{S}_e,n+1}^{k+1} = q_{\mathscr{S}_e,n+1}^{\mathrm{tr},(k+1)}$$

$$p_{\mathscr{S}_e,n+1}^{k+1} = p_{\mathscr{S}_e,n+1}^{\mathrm{tr},(k+1)}$$

$$\zeta_{e,n+1}^{k+1} = \zeta_{e,n}$$

$$\boldsymbol{K}_d^{\mathrm{e}} = -\,\boldsymbol{K}_{\zeta d}^{e}$$

$$K_\zeta^{\mathrm{e}} = 0$$

ENDIF

7.5. Numerical implementation of localization condition

The numerical implementation of the localization condition in (75), which is checked at each Gauss point, is as follows:

$$\texttt{IF} \left| \frac{\|\boldsymbol{s}_{n+1}\|}{\sqrt{2} r_{n+1}} - \sqrt{\frac{3}{3-b^2}} \right| \leqslant h^{\text{tol}} \text{ at a Gauss point,}$$

$$\texttt{THEN} \quad \text{the element has localized} \tag{125}$$

where $h^{\text{tol}} = 1 \times 10^{-5}$ unless otherwise noted.

8. Numerical example: slope stability problem

A slope stability problem is now presented to demonstrate the ability of the model to represent localized deformation in a classic geotechnical structure, an embankment (or slope), in a nearly mesh-independent manner. For simple model problems such as uniform compression, the strong discontinuity approach has been shown to lead to mesh-independent finite element solutions when localized deformation is present [77,78].

Material parameters are shown in Table 1 for three cases: associative deviatoric plastic flow (J2 flow, or von Mises plasticity), non-associative deviatoric plastic flow, and non-associative dilative plastic flow. A gravity load is first applied, the displacements are reset to zero, and a downward displacement is prescribed at the middle of a rigid footing resting at the crest of the slope. The downward displacement may represent the settlement due to a structure placed at the crest of the slope. It is desirable to run a strain-driven problem like this one because otherwise an arc-length method would be needed to advance the solution into and within the softening regime. The dimensions and boundary conditions of the problem are designated in Fig. 6. This is a fictitious example and not an attempt to model the behavior of an actual soil embankment, although the material parameters are chosen to approximately represent those of a soil. Two meshes with 400 and 1600 linear quadrilateral elements are used to analyze the problem.

Fig. 7 shows deformed meshes at end of loading for the standard and enhanced solutions for associative, deviatoric plastic flow. The scale factor for displacements of deformed meshes is 1.0.

Table 1
Material parameters for slope stability problem

E	10 MPa
v	0.4
$\bar{c}$	50, 20, 20 kPa
$\bar{\phi}$	0°, 30°, 30°
b	0.0, 0.0, 0.2
H', K'	0
H_δ, K_δ	− 200 kPa/m
γ	20 kN/m^3

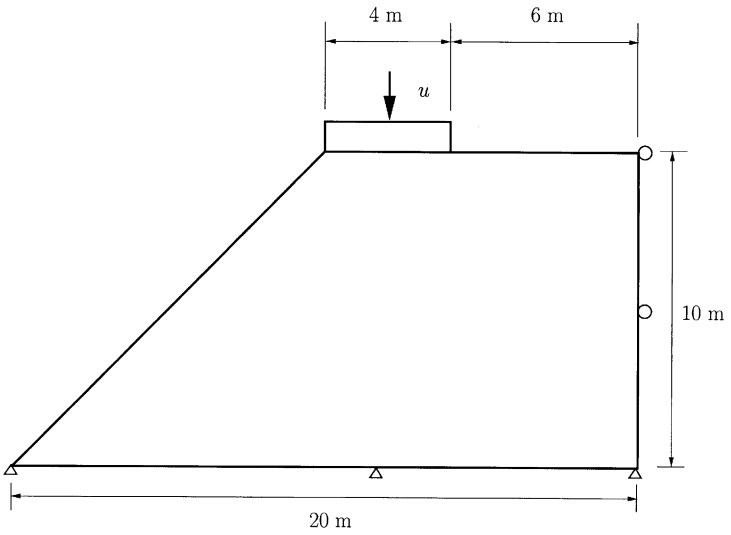

Fig. 6. Slope stability problem. Gravity load applied before footing displacement u is prescribed.

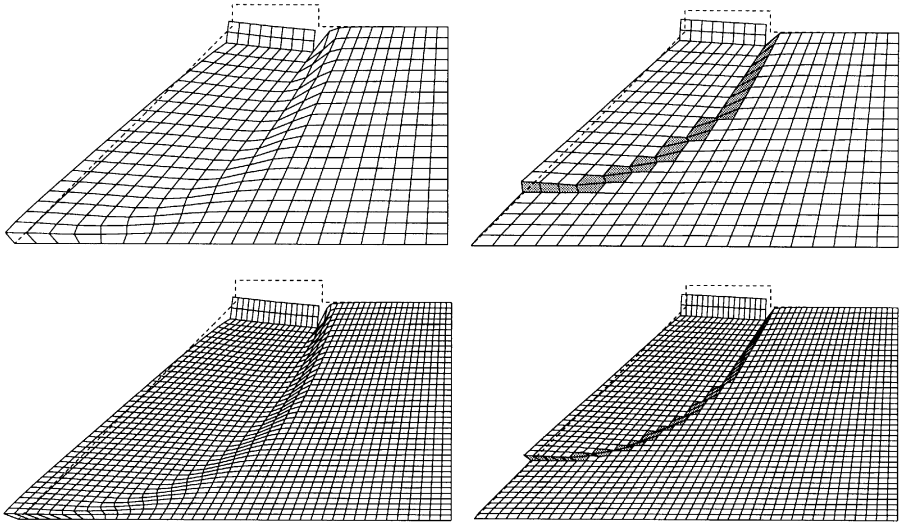

Fig. 7. Deformed meshes for standard and enhanced solutions with associative, deviatoric plactic flow: $\beta = b = 0.0$. 400 and 1600 linear quadrilateral elements with $\bar{B}$. Localized elements are shaded.

Note the diffuse deformation patterns for the standard solutions and the sharp localized deformation for the enhanced solutions. Shaded elements are those through which the slip line has traced. Insensitivity to mesh alignment is demonstrated by the slip line tracing across elements without element sides being aligned with the slip line orientation and by slip lines having the same

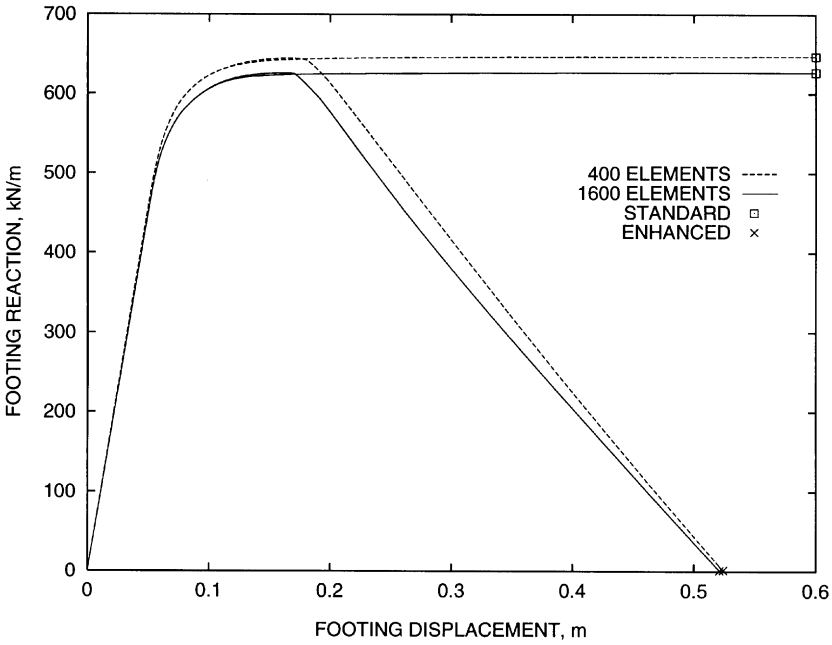

Fig. 8. Load–displacement plots for associative, deviatoric plastic flow: $\beta = b = 0.0$. $h^{\text{tol}} = 1 \times 10^{-5}$. Similar softening slopes of enhanced solution curves demonstrate near-objectivity with respect to mesh refinement.

orientation for the 400 and 1600 element meshes. The slip line initiates in the element just to the right of the rigid footing corresponding with the load at which the standard and enhanced solution curves begin to deviate from one another as seen in Figs. 8, 10, and 12. The load at which the enhanced solution curve begins to soften corresponds with the load at which the slip line has fully propagated through the mesh.

Load–displacement plots for associative, deviatoric plastic flow are shown in Fig. 8. The $\bar{B}$-method [79] is used to address potential mesh-locking due to incompressible plastic flow for small deformations and rotations. Similar slopes of the enhanced solution curves demonstrate near-objectivity with respect to mesh refinement. The standard solution curves demonstrate the well-known mesh dependence for perfect plasticity. Associative, deviatoric plastic flow may be used to simulate the behavior of a saturated cohesive soil in undrained condition (i.e. incompressible for immediate loading).

Fig. 9 shows deformed meshes at end of loading for the standard and enhanced solutions for non-associative, deviatoric plastic flow. The $\bar{B}$-method is used to address potential mesh-locking due to incompressible plastic flow for small deformations and rotations. Again, note the diffuse deformation patterns for the standard solutions and the sharp localized deformation for the enhanced solutions. Load–displacement plots for non-associative, deviatoric plastic flow are shown in Fig. 10. Similar slopes of the enhanced solution curves demonstrate near-objectivity with respect to mesh refinement. The standard solution curves demonstrate the well-known mesh dependence for perfect plasticity.

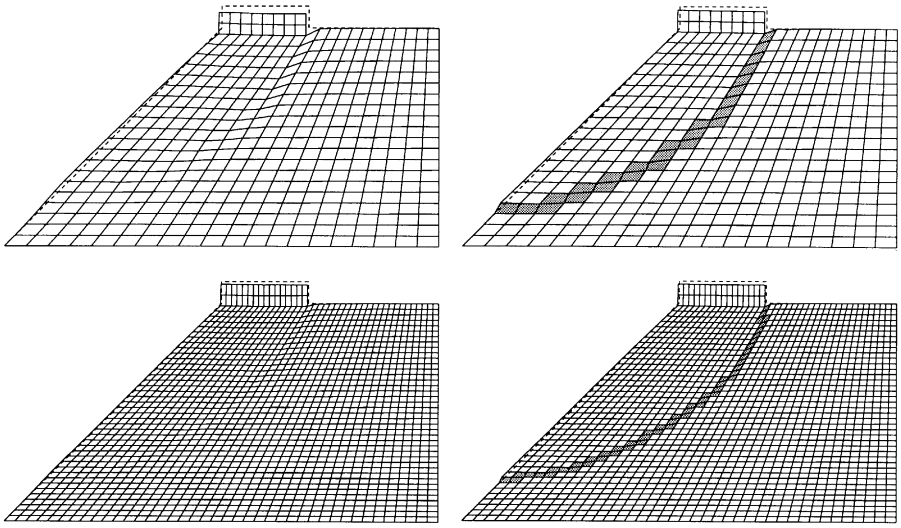

Fig. 9. Deformed meshes for standard and enhanced solutions with non-associative, deviatoric plactic flow: $\beta = 0.5, b = 0.0$. 400 and 1600 linear quadrilateral elements with $\bar{B}$. Localized elements are shaded.

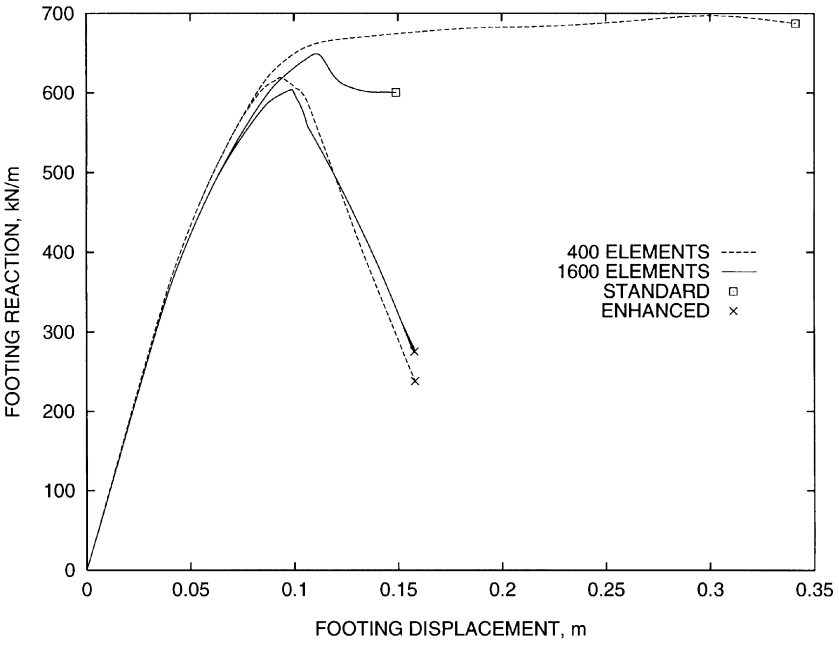

Fig. 10. Load–displacement plots for non-associative, deviatoric plastic flow: $\beta = 0.5, b = 0.0$. $h^{\text{tol}} = 5 \times 10^{-5}$. Similar softening slopes of enhanced solution curves demonstrate near-objectivity with respect to mesh refinement.

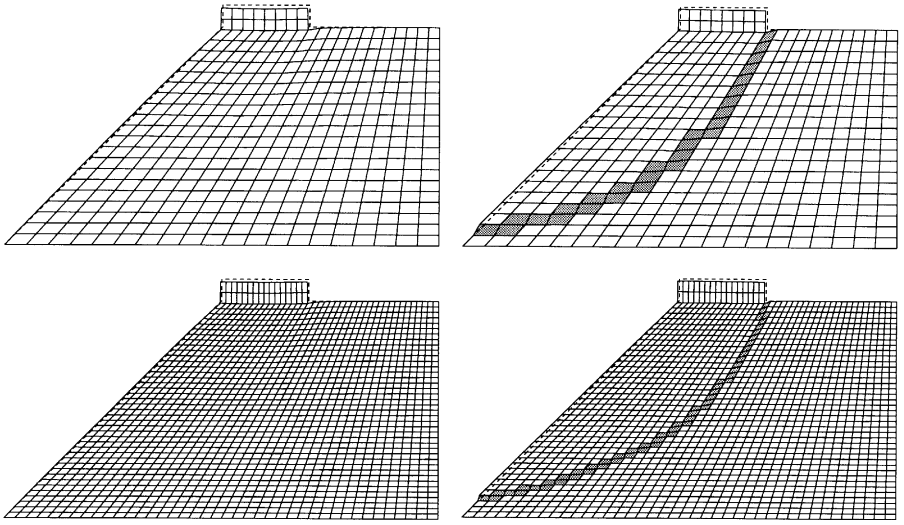

Fig. 11. Deformed meshes for standard and enhanced solutions with non-associative, dilative plactic flow: $\beta = 0.5, b = 0.2$. 400 and 1600 linear quadrilateral elements. Localized elements are shaded.

Fig. 11 shows deformed meshes at the end of loading for the standard and enhanced solutions for non-associative, dilative plastic flow. Standard 2×2 numerical integration is used. Again, note the diffuse deformation patterns for the standard solutions and the sharp localized deformation for the enhanced solutions. Also note the different slip-line curvatures in Figs. 9 and 11. The slip lines in Fig. 11 have a larger radius of curvature than the slip lines in Fig. 9. This is due to the different dilation constants used in each case. Load-displacement plots for non-associative, dilative plastic flow are shown in Fig. 12. Similar slopes of the enhanced solution curves demonstrate near-objectivity with respect to mesh refinement. The standard solution curves demonstrate the well-known mesh dependence for perfect plasticity.

9. Closure

In summary, a rate-independent, non-associated, strain-softening Drucker–Prager plasticity model has been formulated in the context of strong discontinuities and implemented along with an enhanced quadrilateral element within the framework of an assumed enhanced strain finite element method. A finite element analysis of localized deformation occurring in a model problem of slope stability has been conducted in a nearly mesh-independent manner. The effect of dilatancy on the orientation of slip lines has been demonstrated for the slope stability problem.

In conclusion, it is important to capture the structural phenomenon of localized deformation and the associated loss of overall material body strength as accurately as possible via a finite element model but to do so in a mesh-independent manner. The strong discontinuity approach provides the framework to satisfy both of these modeling requirements and does so without special treatments such as a material length scale or adaptive remeshing strategy.

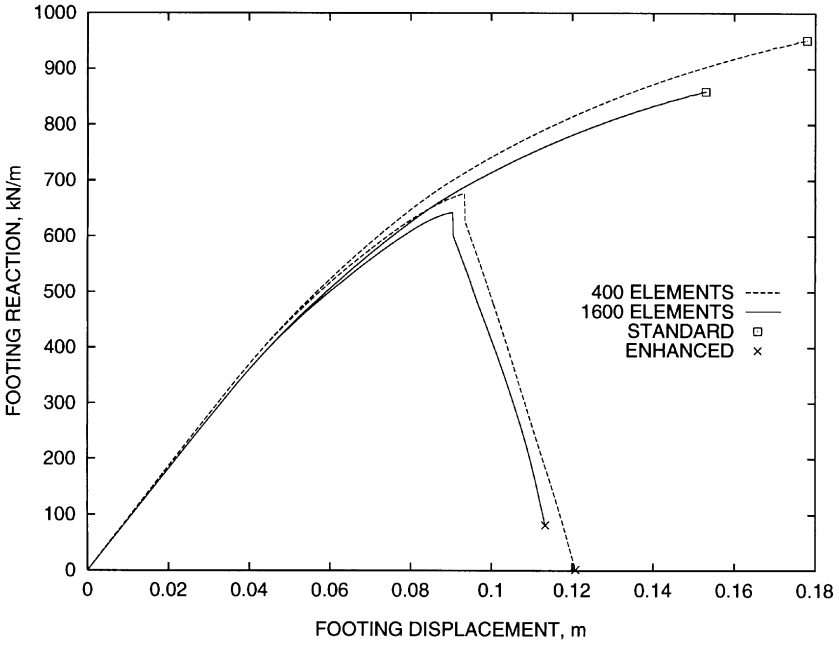

Fig. 12. Load–displacement plots for non-associative, dilative plastic flow: $\beta = 0.5, b = 0.2$. $h^{\text{tol}} = 5 \times 10^{-5}$. Similar softening slopes of enhanced solution curves demonstrate near-objectivity with respect to mesh refinement.

Future work includes extending the model for three-dimensional analysis and incorporating the fluid phase and nonlinear geometric effects to be able to model the behavior of realistic, in situ geomechanical structures which are susceptible to developing localized deformation.

Acknowledgements

The work presented in this paper was supported by the G3S Division of the National Science Foundation through Grant No. CMS97-00426 under the directorship of Dr. Priscilla P. Nelson. This support is gratefully acknowledged.

References

[1] N. Janbu, Stability analysis of slopes with dimensionless parameters, Harvard Univ. Soil Mech. Ser. 46 (1954) 1–81.
[2] W.M. Enger (Rear Admiral), Design Manual: Soil Mechanics, Foundations, and Earth Structures, NAVFAC DM-7, March 1971.
[3] I. Vardoulakis, M. Goldschieder, G. Gudehus, Formation of shear bands in sand bodies as a bifurcation problem, Int. J. Numer. Anal. Methods Geomech. 2 (1978) 99–128.
[4] I. Vardoulakis, M. Goldschieder, Biaxial apparatus for testing shear bands in soils, in: Soil Mechanics and Foundation Engineering, A.A. Balkema, Rotterdam, 1981, pp. 819–824.

[5] D.K. Hallbauer, H. Wagner, N.G.W. Cook, Some observations concerning the microscopic and mechanical behaviour of quartzite specimens in stiff, triaxial compression tests, Int. J. Rock Mech. Mining Sci. Geomech. Abstr. 10 (1973) 713–726.
[6] F.J. Santarelli, E.T. Brown, Failure of three sedimentary rocks in triaxial and hollow cylinder compression tests, Int. J. Rock Mech. Mining Sci. Geomech. Abstr. 26 (1989) 401–413.
[7] W.R. Wawersik, J.W. Rudnicki, W.A. Olsson, D.J. Holcomb, K.T. Chau, Localization of deformation in brittle rock: theoretical and laboratory investigations, in: S.P. Shah, S.E. Swartz, M.L. Wang (Eds.), Micromechanics of Failure of Quasi-Brittle Materials, Elsevier, New York, 1990, pp. 115–124.
[8] A. Ord, I. Vardoulakis, R. Kajewski, Shear band formation in Gosford sandstone, Int. J. Rock Mech. Mining Sci. Geomech. Abstr. 28 (1991) 397–409.
[9] M. Yumlu, M.U. Ozbay, A study of the behaviour of brittle rocks under plane strain and triaxial loading conditions, Int. J. Rock Mech. Mining Sci. Geomech. Abstr. 32 (1995) 725–733.
[10] J.F. Labuz, S.-T. Dai, E. Papamichos, Plane-strain compression of rock-like materials, Int. J. Rock Mech. Mining Sci. Geomech. Abstr. 33 (1996) 573–584.
[11] H.E. Read, G.A. Hegemier, Strain softening of rock, soil, and concrete — A review article, Mech. Mater. 3 (1984) 271–294.
[12] P.A. Cundall, O.D.L. Strack, A discrete numerical model for granular assemblies, Géotechique 29 (1979) 47–65.
[13] P.A. Cundall, Numerical experiments on localization in frictional materials, Ing.-Arch. 59 (1989) 148–159.
[14] J.P. Bardet, M. Proubet, A numerical investigation of the structure of persistent shear bands in granular media, Géotechnique 41 (1991) 599–613.
[15] R.I. Borja, J.R. Wren, Micromechanics of granular media, Part I: Generation of overall constitutive equation for assemblies of circular disks, Comput. Methods Appl. Mech. Eng. 127 (1995) 13–36.
[16] J.R. Wren, R.I. Borja, Micromechanics of granular media, Part II: overall tangential moduli and localization model for periodic assemblies of circular disks, Comput. Methods Appl. Mech. Eng. 141 (1997) 221–246.
[17] J.H. Prevost, K. Höeg, Soil mechanics and plasticity analysis of strain softening, Géotechnique 25 (1975) 279–297.
[18] I.S. Sandler, J.P. Wright, Strain-softening, in: S. Nemat-Nasser, R. Asaro, G. Hegemier (Eds.), Theoretical Foundations for Large Scale Computations of Nonlinear Material Behavior, Martinus Nijhoff, The Netherlands, 1984, pp. 285–315.
[19] J. Hadamard, Leçons sur la Propagation des Ondes et les Équations de L'Hydrodynamique, Librairie Scientifique A, Hermann, Paris, 1903.
[20] T.Y. Thomas, Plastic Flow and Fracture in Solids, Academic Press, New York, 1961.
[21] R. Hill, Acceleration waves in solids, J. Mech. Phys. Solids 10 (1962) 1–16.
[22] J. Mandel, Conditions de stabilité et postulat de Drucker, in: J. Kravtchenko, P.M. Sirieys (Eds.), Rheology and Soil Mechanics, Springer, Berlin, 1966, pp. 58–68.
[23] J.R. Rice, The localization of plastic deformation, in: W.T. Koiter (Ed.), Theoretical and Applied Mechanics, North-Holland, Amsterdam, 1976, pp. 207–220.
[24] S.T. Pietruszczak, Z. Mróz, Finite element analysis of deformation of strain-softening materials, Int. J. Numer. Methods Eng. 17 (1981) 327–334.
[25] Z.P. Bažant, F.-B. Lin, Non-local yield limit degradation, Int. J. Numer. Methods Eng. 26 (1988) 1805–1823.
[26] J. Oliver, A consistent characteristic length for smeared cracking models, Int. J. Numer. Methods Eng. 28 (1989) 461–474.
[27] O.C. Zienkiewicz, G.C. Huang, A note on localization phenomena and adaptive finite-element analysis in forming processes, Commun. Appl. Numer. Methods 6 (1990) 71–76.
[28] O.C. Zienkiewicz, M. Pastor, M. Huang, Softening, localisation and adaptive remeshing, Capture of discontinuous solutions, Comput. Mech. 17 (1995) 98–106.
[29] T.J.R. Hughes, Multiscale phenomena: Green's functions, the Dirichlet-to-Neumann formulation, subgrid scale models, bubbles and the origins of stabilized methods, Comput. Methods Appl. Mech. Eng. 127 (1995) 387–401.
[30] K.R. Garikipati, T.J.R. Hughes, A study of strain localization in a multiple scale framework—the one dimensional problem, Comput. Methods Appl. Mech. Eng. 159 (1998) 193–222.
[31] M. Ortiz, I. Leroy, A. Needleman, A finite element method for localized failure analysis, Comput. Methods Appl. Mech. Eng. 61 (1987) 189–214.

[32] T. Belytschko, J. Fish, E. Engelmann, A finite element with embedded localization zones, Comput. Methods Appl. Mech. Eng. 70 (1988) 59–89.
[33] A. Needleman, Material rate dependence and mesh sensitivity in localization problems, Comput. Methods Appl. Mech. Eng. 67 (1988) 69–85.
[34] A. Nacar, A. Needleman, M. Ortiz, A finite element method for analyzing localization in rate dependent solids at finite strains, Comput. Methods Appl. Mech. Eng. 73 (1989) 235–258.
[35] B. Loret, J.H. Prevost, Dynamic strain localization in elasto-(visco)-plastic solids, Part 1. General formulation and one-dimensional examples, Comput. Methods Appl. Mech. Eng. 83 (1990) 247–273.
[36] J.H. Prevost, B. Loret, Dynamic strain localization in elasto-(visco)-plastic solids, Part 2. Plane strain examples, Comput. Methods Appl. Mech. Eng. 83 (1990) 275–294.
[37] L.J. Sluys, R. de Borst, Wave propagation and localization in a rate-dependent cracked medium—Model formulation and one-dimensional examples, Int. J. Solids Struct. 29 (1992) 2945–2958.
[38] E.C. Aifantis, On the microstructural origin of certain inelastic models, J. Eng. Mater. Technol., ASME 106 (1984) 326–330.
[39] R. de Borst, J. Pamin, Some novel developments in finite element procedures for gradient-dependent plasticity, Int. J. Numer. Methods Eng. 39 (1996) 2477–2505.
[40] E. Cosserat, F. Cosserat, Théorie des Corps Déformables, Librairie Scientifique A. Hermann et Fils, Paris, 1909.
[41] R.D. Mindlin, Influence of couple-stresses on stress concentrations, Exp. Mech. 3 (1963) 1–7.
[42] R. de Borst, L.J. Sluys, Localisation in a Cosserat continuum under static and dynamic loading conditions, Comput. Methods Appl. Mech. Eng. 90 (1991) 805–827.
[43] J.C. Simo, J. Oliver, F. Armero, An analysis of strong discontinuities induced by strain- softening in rate-independent inelastic solids, Comput. Mech. 12 (1993) 277–296.
[44] J.C. Simo, J. Oliver, A new approach to the analysis and simulation of strain softening in solids, in: Z.P. Bažant, Z. Bittnar, M. Jirásek, J. Mazars (Eds.), Fracture and Damage in Quasibrittle Structures, E&FN Spon, London, 1994, pp. 25–39.
[45] F. Armero, K. Garikipati, Recent advances in the analysis and numerical simulation of strain localization in inelastic solids, in: D.R.J. Owen, E. Oñate, E. Hinton (Eds.), Proceedings of Computational Plasticity IV, CIMNE, Barcelona, Spain, 1995, pp. 547–561.
[46] F. Armero, K. Garikipati, An analysis of strong discontinuities in multiplicative finite strain plasticity and their relation with the numerical simulation of strain localization in solids, Int. J. Solids Struct. 33 (1996) 2863–2885.
[47] K.R. Garikipati, On strong discontinuities in inelastic solids and their numerical simulation, Ph.D. Thesis, Stanford University, 1996.
[48] R.G. Wan, D.H. Chan, N.R. Morgenstern, A finite element method for the analysis of shear bands in geomaterials, Finite Elements. Anal. Des. 7 (1990) 129–143.
[49] R. Larsson, K. Runesson, N.S. Ottosen, Discontinuous displacement approximation for capturing plastic localization, Int. J. Numer. Meth. Eng. 36 (1993) 2087–2105.
[50] R. Larsson, K. Runesson, S. Sture, Embedded localization band in undrained soil based on regularized strong discontinuity—Theory and FE-Analysis, Int. J. Solids Struct. 33 (1996) 3081–3101.
[51] L.M. Kachanov, Foundations of the Theory of Plasticity, North-Holland, Amsterdam, 1971.
[52] R.I. Borja, R.A. Regueiro, Strain localization in frictional materials exhibiting displacement jumps, Comput. Methods Appl. Mech. Eng., in review.
[53] R.A. Regueiro, Finite element analysis of strain localization in geomaterials taking a strong discontinuity approach, Ph.D. Thesis, Stanford University, 1998.
[54] T.J.R. Hughes, The Finite Element Method, Prentice-Hall, Englewood Cliffs, NJ, 1987.
[55] L.E. Malvern, Introduction to the Mechanics of a Continuous Medium, Prentice-Hall, Englewood Cliffs, NJ, 1969.
[56] H. Matthies, G. Strang, E. Christiansen, The saddle point of a differential program, in: R. Glowinski, E.Y. Rodin, O.C. Zienkiewicz (Eds.), Energy Methods in Finite Element Analysis, Wiley, New York, 1979, pp. 309–318.
[57] R. Temam, G. Strang, Functions of bounded deformation, Arch. Rat. Mech. Anal. 75 (1980) 7–21.
[58] G. Strang, H. Matthies, R. Temam, Mathematical and computational methods in plasticity, in: S. Nemat-Nasser (Ed.), Variational Methods in the Mechanics of Solids, Pergamon Press, Oxford, 1980, pp. 20–28.

[59] P.-M. Suquet, Existence and regularity of solutions for plasticity problems, in: S. Nemat-Nasser (Ed.), Variational Methods in the Mechanics of Solids, Pergamon Press, Oxford, 1980, pp. 304–309.
[60] I. Stakgold, Green's Functions and Boundary Value Problems, 2nd edition, Wiley, New York, 1998.
[61] J.C. Simo, T.J.R. Hughes, Computational Inelasticity, Springer, New York, 1998.
[62] J. Lubliner, Plasticity Theory, Macmillan, New York, 1990.
[63] D.C. Drucker, A more fundamental approach to plastic stress-strain relations, in: Proceedings of the first US National Congress in Applied Mechanics, ASME, 1951, pp. 487–491.
[64] P.A. Vermeer, R. de Borst, Non-associated plasticity for soils, concrete, and rock, Heron 29 (1984) 3–64.
[65] J.C. Simo, Topics on the numerical analysis and simulation of plasticity, in: P.G. Ciarlet, J.L. Lions (Eds.), Handbook of Numerical Analysis, Vol. III, Elsevier, New York, 1996.
[66] J.W. Rudnicki, J.R. Rice, Conditions for the localization of deformation in pressure-sensitive dilatant materials, J. Mech. Phys. Solids 23 (1975) 371–394.
[67] J.C. Simo, R.L. Taylor, Consistent tangent operators for rate-independent elastoplasticity, Comput. Methods Appl. Mech. Eng. 48 (1985) 101–118.
[68] D.C. Drucker, W. Prager, Soil mechanics and plastic analysis or limit design, Q. Appl. Math. 10 (1952) 157–165.
[69] D.R.J. Owen, E. Hinton, Finite Elements in Plasticity: Theory and Practice, Pineridge, Swansea, 1980.
[70] D. Radenkovic, Théorèmes limites pour un matériau de Coulomb à dilatation non standardisée, C.R. Séances Acad. Sci. 252 (1961) 4103–4104.
[71] J.W. Rudnicki, The inception of faulting in a rock mass with a weakened zone, J. Geophys. Res. 82 (1977) 844–854.
[72] J.E. Marsden, T.J.R. Hughes, Mathematical Foundations of Elasticity, Prentice-Hall, Englewood Cliffs, NJ, Dover edition, 1994.
[73] K.H. Roscoe, The influence of strain in soil mechanics, 10th Rankine Lecture, Géotechnique 20 (1970) 129–170.
[74] J. Atkinson, An Introduction to the Mechanics of Soils and Foundations Through Critical State Soil Mechanics, McGraw-Hill, New York, 1993.
[75] J.C. Simo, M.S. Rifai, A class of mixed assumed strain methods and the method of incompatible modes, Int. J. Numer. Methods Eng. 29 (1990) 1595–1638.
[76] R.L. Taylor, J.C. Simo, O.C. Zienkiewicz, A.C.H. Chan, The patch test — a condition for assessing FEM convergence, Int. J. Numer. Methods Eng. 22 (1986) 39–62.
[77] R.A. Regueiro, T.Y. Lai, R.I. Borja, Computational modeling of strain localization in soft rock, in: The Geotechnics of Hard Soils – Soft Rocks, Proc. 2nd Int. Symp. Naples, Italy, (Eds.) A. Evangelista, L. Picarelli, Balkema, Rotterdam, 1998, pp. 789–797.
[78] R.I. Borja, R.A. Regueiro, T.Y. Lai, FE modeling of strain localization in soft rocks, J. Geotech. Geoenv. Eng., 1998, in review.
[79] T.J.R. Hughes, Generalization of selective integration procedures to anisotropic and nonlinear media, Int. J. Numer. Methods Eng. 15 (1980) 1413–1418.